218

A new sub grid scale orographic drag parametrization: Its formulation and testing

F. Lott and M.J. Miller

Research Department

July 1995

SUMMARY

A scheme for the representation of Sub-grid Scale Orography (SSO) in NWP and climate models is presented. It arose in part from a desire to represent nonlinear low level mountain drag effects not currently parametrized. An important feature of the scheme is that it deals explicitly with low-level flow which is "blocked", when the effective height of the sub-grid scale orography is high enough. In this new scheme, it is assumed that for this "blocked" flow, separation occurs at the mountain flanks resulting in a form drag. This drag is parametrized on model levels which are intersected by the SSO, and provides a dynamically based replacement for envelope orography. The upper part of the low level flow goes over the orography and generates gravity waves. The different parameters of the scheme are adjusted, using an off-line procedure in which the scheme is used to estimate the mountain drag and the momentum profiles above the Pyrenees and these estimates are validated with the PYREX data. T106 and T213 forecasts with this new scheme and with mean orography show that the forecast mountain drag consistently reproduces the drag measured during PYREX. Isentropic flow diagnostics further show that the new scheme has a realistic impact on the flow dynamics, reinforcing the low-level wake observed in mesoscale analyses of the flow. With this new scheme and a mean orography, the ECMWF model outperforms a version of the model which has an envelope orography and the old gravity wave drag scheme in terms of forecast skill, while no longer suffering any disadvantages of envelope orography. The proposed low-level drag parametrization should also be relevant at much higher model horizontal resolutions than T213.

1. INTRODUCTION

In many of the studies concerning the representation of orography in Numerical Weather Prediction (NWP) and General Circulation (GCM) models, attention has been focused either on the parametrization of sub-grid scale mountain waves or on the optimal representation of the resolved mountain ranges. The first approach has led to the introduction of the gravity wave drag schemes (*Boer et al*, 1984; *Palmer et al*, 1986; *Miller et al*, 1989) and the second to the use of an envelope orography, for example, which improves the model representation of the large scale planetary waves (*Wallace et al*, 1983). These studies dealt essentially with the impact of the sub-grid scale orography and of the resolved scale orography on the global dynamics of the atmosphere. Recent studies of the local behaviour of the ECMWF model near the Pyrenees (*Lott*, 1995) have shown that the model underestimates the mountain drag, and generates mountain waves, with a horizontal scale close to the model truncation and which are often not observed. Furthermore, the way these waves are dissipated and affect the flow is unclear and unrealistic. These results are surprising since envelope orography increases the height and volume of the orography, and increases the drag on the atmosphere (*Tibaldi*, 1986). The envelope orography, however, is detrimental to the data assimilation process since more low level data, located below the model ground, are rejected using an envelope orography. Envelope orography also tends to give excessive precipitation, especially from convection generated by the elevated heating of the enhanced orography. It may therefore be desirable to replace the envelope orography by a mean orography without further changes but such a reduction of the mountain height will reduce the model mountain pressure drag with detrimental effect on the forecasts and model climate. The fact that the present gravity wave drag scheme inadequately represents low level drag, and the fact that the total mountain drag is already too small in the current model with envelope orography indicate that a major revision of the representation of Sub-grid Scale Orography (SSO) is desirable, and necessary to successfully represent the overall impact of orography on the global dynamics. *Clark and Miller* (1991) have shown, using a nested high resolution model, that there is a large underestimation of the total drag at horizontal resolutions coarser than about 10 km, which cannot adequately be made up by the use of an envelope orography.

Recent work by *Baines and Palmer* (1990) presents the principles of a sub-grid scale orographic drag scheme in which particular emphasis is placed on the representation of three-dimensional wave surface stress. These authors also suggested that further drag should be provided at model levels which intersect the sub-grid scale orography. The following sections propose a theoretical formulation for such a drag on model levels and this forms a major component of the new sub-grid scale orographic drag scheme. The general principles are presented in section 2, interpreting results from theoretical studies of flow near mesoscale orography in the context of numerical weather prediction models. Section 3 describes the parametrization scheme in detail. In section 4, using an off-line procedure, the new scheme is used to predict the drag and the momentum flux profiles, observed during the PYREX experiment. Section 5 of the paper presents an on-line validation of the scheme. The scheme is tested with the ECMWF model (at T106 and T213 resolutions), using forecast experiments covering the Periods of Intense Observation of the PYREX campaign. At both resolutions, it appears that the model with the new scheme is consistently able to reproduce the measured pressure drag. Isentropic diagnostics of the flow dynamics are used to study the impact of the scheme on the low level flow dynamics. Section 6 summarizes some experimental forecast results comparing performances of the model

with mean orography with and without the new scheme, and with a version of the model with envelope orography and the old gravity wave drag scheme that has been used operationally at ECMWF.

2.   GENERAL PRINCIPLES OF THE NEW SCHEME

The new scheme uses ideas presented by *Baines and Palmer* (1990) combined with ideas based on bluff body dynamics. It assumes that the mesoscale flow dynamics can be described by two conceptual models, the relevance of which depends on the non-dimensional height of the mountain,

$$H_N = \frac{NH}{|U|} \qquad (1)$$

where H is the maximum height of the obstacle, U and N are the wind speed and the Brunt-Viasala frequency of the incident flow respectively.

At small H_N, all the flow goes over the mountain and gravity waves are forced by the vertical motion of the fluid. Assuming that the mountain has the shape of a single elliptic mountain with height variation determined by the parameter b in the along ridge direction and by the parameter a in the cross ridge direction such that $\gamma = a/b \leq 1$, then the geometry of the mountain can be written as:

$$h(x,y) = \frac{H}{1 + \frac{x^2}{a^2} + \frac{y^2}{b^2}}. \qquad (2)$$

In the simple case when the incident flow is perpendicular to the ridge the gravity wave surface stress has the magnitude,

$$\tau_w = \rho_0 \, b \, G \, B(\gamma) \, NUH^2 \qquad (3)$$

assuming that the Boussinesq and the hydrostatic approximations are valid. In Eq (3), G is a function of the mountain sharpness (*Phillips*, 1984), and $G \sim 1.23$, for the mountain given by Eq (2). The constant $B(\gamma)$ is a function of the mountain anisotropy, γ, varying from $B(0)=1$ for a two-dimensional ridge to $B(1)= \pi/4$, for a circular mountain.

At large H_N, the vertical motion of the fluid is limited and part of the low level flow goes around the mountain. As explained in section 3, the depth of this blocked layer when U and N are independent of height can be expressed as,

$$Z_b = H \frac{(H_N - H_{NC})}{H_N} \qquad (4)$$

where H_{NC} is a critical non-dimensional mountain height of order unity. The depth Z_b can be viewed as the upstream elevation of the isentropic surface that is raised exactly to the mountain top (Fig 1). In each layer

below Z_b the flow streamlines split around the obstacle, and it is assumed that flow separation occurs on the obstacle's flanks. Then, the drag exerted by the obstacle on the flow at these levels can be written as,

$$D_b(z) = - \rho_0 \, C_d \, l(z) \, \frac{U|U|}{2}. \tag{5}$$

Here $l(z)$ is a length scale characterizing the horizontal extension of the obstacle as seen by the flow with upstream altitude z, and C_d is a constant close to unity according to the theory of jets in ideal fluids (*Kirchoff*, 1876; *Gurevich*, 1965). According to observations, C_d can be nearer two when suction effects occur in the rear of the obstacle (*Lamb*, 1932). In the proposed parametrization scheme, this drag is applied to the flow level by level, and will be referred to as the drag of the "blocked" flow, D_b. Unlike the gravity wave drag scheme, the total stress exerted by the mountain on the "blocked" flow does not need to be known "a priori". For an elliptic mountain, the length of the obstacle as seen by the flow at a given altitude z is given by,

$$l(z) = 2b \, \sqrt{\frac{Z_b - z}{z}}. \tag{6}$$

In Eq (6), it assumed the level Z_b is raised up to the mountain top, with each layer below Z_b raised by a factor H/Z_b (Fig 1). This leads to a reduction of the obstacle length effectively seen by the the flow when compared to the case for which the flow does not experience vertical motion as it approaches the mountain. Then, applying Eq (5) to the fluid layers below Z_b, the stress due to the blocked flow drag is obtained by integration from $z=0$ to $z=Z_b$:

$$\tau_b \sim C_d \, \pi b \, \rho_0 \, Z_b \frac{U|U|}{2}. \tag{7}$$

However, when the non-dimensional height is close to unity, the presence of a wake is generally associated with upstream blocking and with a downstream foehn (e.g. Fig 1). This means that the isentropic surfaces are lifted on the windward side and descend close to the ground on the leeward side. Assuming that the lowest isentropic surface passing over the mountain can be viewed as a lower rigid boundary for the flow passing <u>over</u> the mountain, the distortion of this surface will be seen as a source of gravity waves. Since this distortion has the same magnitude as the mountain height, it is assumed that the wave stress is given by Eq (3), whatever the depth of the blocked flow, Z_b. Then, when the non-dimensional mountain height is larger than H_{NC}, the total stress can be written:

$$\tau \sim \tau_w \left(1 + \frac{\pi C_d}{2 \, G \, B(\gamma)} \frac{H_N - H_{NC}}{H_N^2} \right). \tag{8}$$

4

When the non-dimensional mountain height is smaller than H_{NC}, the total stress is only the gravity wave stress. The addition of low level drag enhances the gravity wave stress in Eq (8) substantially: Fig 2 shows the ratio between the total stress and the wave stress as a function of H_N for two pairs of parameters (C_d, H_{NC}) compared to the pressure drag measured in two numerical experiments of uniform stratified flow incident over (i) a two-dimensional ridge (*Stein*, 1992) and (ii) a three-dimensional ridge (*Miranda and James*, 1992). In these comparisons, it is assumed that the nonlinear enhancement of the drag observed in the two-dimensional simulations represents the drag enhancement one should observe for a flow perpendicular to a very elongated ridge. In the comparison of Eq (8) with the results of *Miranda and James* (1992) it is assumed that differences in the mountain shape used by these authors and that given in Eq (2) may be neglected. Fig 2 shows that two-dimensional drags are well estimated by this conceptual model for C_d=2., H_{NC}=0.4. Since there is substantial upstream blocking in these two-dimensional simulations when the non-dimensional height H_N exceeds two (*Stein*, 1992), the large value of C_d simulates this upstream blocking. Three-dimensional drag values are approached by this conceptual model for C_d=1., H_{NC}=0.75. In this case, the smaller value of C_d is probably related to the reduction of the upstream blocking in three-dimensional simulations. Larger H_{NC} corresponds to a reduction of the nonlinear effects due to the three-dimensional dispersion of the mountain waves. In the new scheme proposed below, these effects will be partly taken into account by allowing the value of C_d to vary with the aspect ratio of the obstacle, as occurs for separated flows around immersed bodies (*Landweber*, 1961) while setting the critical number, H_{NC}=0.5, as a constant intermediate value. Note also that for large H_N Eq (8) overestimates the drag in the 3D case, due to the fact that the flow dynamics become more and more horizontal and the excitation of gravity waves is reduced accordingly. This is not taken into account in the new parametrization scheme partly because a large non-dimensional mountain height often corresponds to slow flows for which the drag given by Eq (8) is then very small in any case.

3. DESCRIPTION OF THE NEW SCHEME.

These ideas have been utilized to represent the effects of SSO in the ECMWF model. Following *Baines and Palmer* (1990), the SSO over one gridpoint region (GPR) is represented by four parameters μ, γ, σ and θ which represents the standard deviation, the anisotropy, the slope of the orography and the geographical orientation of the orography. These four parameters are calculated from the US Navy (10'x10') dataset (see Appendix for details).

The scheme uses values of low-level wind velocity and static stability and these are partitioned in two parts. The first part corresponds to the incident flow which passes over the mountain top, and is evaluated by averaging the wind, the Brunt-Vaisala frequency and the fluid density between μ and 2μ above the model mean orography. Following *Wallace et al* (1983), 2μ is interpreted as the envelope of the sub-grid scale mountain peaks, above the model orography. The wind, the Brunt-Vaisala frequency and the density of this part of the low level flow will be labelled as U_H, N_H and ρ_H respectively. The second part is the "blocked" flow, and its evaluation is based on a very simple interpretation of the non-dimensional mountain height H_N. To first order in the mountain amplitude, the obstacle excites a wave, and the sign of the vertical displacement of a parcel is controlled in the vertical direction by the wave phase. If a fluid parcel ascends the upstream mountain flank over a height large enough to significantly modify the wave phase, its vertical displacement can become zero, and it cannot cross the mountain summit. In this case, the blocking height Z_b, is the highest level located below the mountain top for which the phase change between Z_b and the mountain top exceeds a critical value F_c,

$$\int_{Z_b}^{3\mu} \frac{N}{U_p} \, dz \geq F_c. \tag{9}$$

In Eq (9), the wind speed, $U_p(z)$, is calculated by resolving the wind, $U(z)$, in the direction of the flow U_H. Then, if the flow veers or backs with height, Eq (9) will be satisfied when the flow becomes perpendicular to U_H. Levels below this "critical" altitude define the low level blocked flow. Eq (9) will also be satisfied below inversion layers, where the parameter N is very large. These two properties allow the new parametrization scheme to mimic the vortex shedding observed when pronounced inversions occur (*Etling*, 1989). The upper limit in Eq (9) was chosen to be 3μ, which is above the sub-grid scale mountain tops. This ensures that the integration of Eq (9) does not lead to an underestimation of Z_b, which can occur due to limited vertical resolution when using an upper limit of 2μ (a better representation of the peak height), and could be relaxed with better vertical resolution.

In the following the drag amplitudes will be estimated, combining formulae valid for elliptic mountains with real orographic data. Considerable simplifications are implied and the calculations are virtually scale analyses relating the different amplitudes to the SSO parameters. Hence the calibration and validation of the new scheme described in Sections 4 and 5 is essential.

3.1 The blocked flow drag

Within a given layer, located below the blocking level Z_b, the drag is given by Eq (5). At a given altitude z, the intersection between the mountain and the layer approximates to an ellipse, of eccentricity

$$(a',b') \sim (a,b)\sqrt{\frac{Z_b-z}{z+\mu}}, \tag{10}$$

where, by comparison with Eq (6), it is also assumed that the level $z=0$ (i.e., the model mean orography) is at an altitude μ above the mountain valleys. Taking into account the flow direction, the length $l(z)$ can be written approximately as:

$$l(z) \sim 2\max(b\cos\psi, a\sin\psi)\sqrt{\frac{Z_b-z}{z+\mu}} \tag{11}$$

where ψ is the angle between the incident flow direction and the normal ridge direction, θ. For one GPR, and uniformly distributed SSO, if the incident flow is normal to the ridge ($\psi=0$), it encounters $L/2a$ obstacles and, if it is parallel to the ridge ($\psi=\pi/2$), it encounters $L/2b$ obstacles where L is the length scale of the GPR. Summing up these contributions the dependence of Eq (11) in a and b can be neglected and the length $l(z)$ becomes:

$$l(z) \sim L\sqrt{\frac{Z_b-z}{z+\mu}}. \tag{12}$$

Furthermore the number of consecutive ridges (i.e. located one after the other in the direction of the flow) depends on the obstacle shape: there are approximately L/2b successive obstacles when the flow is along the ridge and $L/2a$, if it is normal to the ridge. Taking this into account together with the flow direction gives:

$$l(z) \sim \frac{L^2}{2}\sqrt{\frac{Z_b-z}{z+\mu}} \ \max \ (\frac{\cos\psi}{a}, \frac{\sin\psi}{b}). \tag{13}$$

Relating the parameters a and b to the SSO parameters: $a \sim \mu/\sigma$, and $a/b \sim \gamma$, and allowing the drag coefficient to vary with the aspect ratio of the obstacle as seen by the incident fluid:

$$r \sim \frac{\cos^2\psi + \gamma\sin^2\psi}{\gamma\cos^2\psi + \sin^2\psi} \tag{14}$$

the drag per unit area can be written:

$$D_b(z) \sim -C_d\max\left(2-\frac{1}{r},0\right)\rho \ \frac{\sigma}{2\mu}\sqrt{\frac{Z_b-z}{z+\mu}} \ \max(\cos\psi, \gamma\sin\psi) \ \frac{U\,|U|}{2}. \tag{15}$$

The drag coefficient is modulated by the aspect ratio of the obstacle to account for the fact that C_d is twice as large for flow normal to an elongated obstacle than for flow round an isotropic obstacle. The drag tends to zero, when the flow is nearly along a long ridge, because flow separation is not expected to occur in such configuration. It can be shown that the term $\max(\cos\psi, \gamma\sin\psi)$ is similar to a later form used for the directional dependence of the gravity wave stress. For simplicity, this later form is adopted:

$$D_b(z) = -C_d \max(2 - \frac{1}{r}, 0)\ \rho\ \frac{\sigma}{2\mu}\ \sqrt{\frac{Z_b - z}{z + \mu}}\ (B\cos^2\psi + C\sin^2\psi)\ \frac{U\ |U|}{2} \qquad (16)$$

where the constants $B(\gamma)$ and $C(\gamma)$ are defined below. The difference between Eq (15) and Eq (16) has been shown to have a negligible impact on any aspect of the model behaviour.

In practice, Eq 16 is suitably resolved and applied to the component form of the horizontal momentum equations. To ensure numerical stability this term is evaluated quasi-implicitly level by level such that large drag values cannot create flow reversal in one timestep.

3.2   The gravity wave drag

This gravity wave part of the scheme is based on *Miller et al* (1989) and *Baines and Palmer* (1990), and takes into account some three-dimensional effects in the wave stress amplitude and orientation. For clarity and convenience, it is briefly described here. Assuming that the SSO has the shape of one single elliptic mountain, the mountain wave stress can be written as (*Phillips*, 1984):

$$(\tau_1, \tau_2) = \rho_H U_H N_H H^2 b\ G\ (\ B\cos^2\psi_H + C\sin^2\psi_H\ ,\ (B - C)\sin\psi_H\cos\psi_H\ ) \qquad (17)$$

where $B = 1 - 0.18\gamma - 0.04\gamma^2$, $C = 0.48\gamma + 0.3\gamma^2$ and G is a constant of order 1. Furthermore, when b or a are significantly smaller than the length L characteristic of the gridpoint region size, there are typically $L^2/4ab$ ridges inside the GPR. Summing all the associated forces gives the stress per unit area,

$$(\tau_1, \tau_2) = \rho_H U_H N_H\ \mu\sigma\ G\ (\ B\cos^2\psi_H + C\sin^2\psi_H\ ,\ (B - C)\sin\psi_H\cos\psi_H\ ) \qquad (18)$$

where H in Eq (17) was replaced by 2μ and a by μ/σ.

It is worth noting that, since the basic parameters ρ_H, U_H, N_H are evaluated for the layer between μ and 2μ above the mean orography that defines the model's lower boundary, there will be much less diurnal cycle in the stress than in previous formulations that used the lowest model levels for this evaluation. The vertical distribution of the gravity wave stress will determine the levels at which the waves break and slow down the synoptic flow. Since this part of the scheme is only active above the blocked flow, this stress is now constant from the bottom model level to the top of the blocked flow, Z_b. Above Z_b, up to the top of the model, the

stress is constant until the waves break. This occurs when the total Richardson number falls below a critical value Ri_c, which is of order 1. When the non-dimensional mountain height is close to unity, this algorithm typically predicts wave breaking at relatively low levels. This is not surprising since the linear theory of mountain gravity waves predicts low level breaking wave at large non-dimensional mountain heights (*Miles and Huppert*, 1969). In reality, the depth over which gravity wave breaking occurs is more likely related to the vertical wavelength of the waves. For this reason, when low level wave breaking occurs in the scheme, the corresponding drag is distributed (above the blocked flow), over a layer of thickness ΔZ, equal to a quarter of the vertical wavelength of the waves, i.e.:

$$\int_{Z_b}^{Z_b + \Delta Z} \frac{N}{U_p} dz \approx \frac{\pi}{2}. \tag{19}$$

Above the height $Z_b + \Delta Z$ are waves with amplitude small enough to continue propagating vertically.

4.   OFF-LINE CALIBRATION

The new scheme essentially depends on the four parameters, C_d, G, Ri_c and F_c. The first two parameters directly control the amplitude of the blocked flow drag and of the gravity wave drag. The third and the fourth parameters control the vertical distribution of these drags. The final forms of Eqs 9, 16 and 18 contain several assumptions and simplification; investigations of the sensitivity of parameter values have therefore been made before testing the scheme in the model. This is done using an off-line calibration in which the SSO scheme is just a predictor of the perpendicular component of the mountain pressure drag, and of the momentum flux vertical profiles which were observed during the PYREX field experiment.

In the following, the incident wind (extracted from the ECMWF re-analysis (*Lott*, 1995) of the data collected during the PYREX campaign (*Bougeault et al*, 1993)) is provided every 6 hours as an input to the new parametrization. For each flow profile the parametrization scheme is used to calculate a mountain drag and a momentum flux profile which can then be compared to the corresponding measurements. This direct comparison is possible when the size of the GPR is close to the PYREX North-South transect length (~150 km), along which the measurements are done. This length is a little larger (20%) than the latitude grid scale of the ECMWF model at T106. This direct comparison is further justified by the fact that at T106, the Pyrenees are virtually unresolved by the model orography, and hence the total mountain drag has to be parametrized. The GPR chosen covers the area [(-1W,1E)x(41.7N,43.3N)], which encloses the Pyrenees. Over this area, the (10'x 10') USN dataset provides 110 values of the orography elevation. This data is displayed in Fig 3 as a function of their longitude. Over this GPR, the SSO parameters have values, $\gamma = 0.63$, $\sigma = 0.0021$, $\theta = 75°$, $\mu = 600$ m and h_m (the model orographic height) $= 930$ m. In Fig 3, the values h_m, $h_m + 2\mu$

and $h_m - \mu$ are also indicated. As mentioned earlier, this example illustrates that the envelope of the peaks correspond well to $h_m + 2\mu$, while the envelope of the valleys is approximated by $h_m - \mu$. The total Sub-grid Scale mountain height is then ~1800 m, which is a good approximation of the Pyrenees elevation. It is smaller than the mountain elevation measured along the PYREX central transect (~2100 m), which is not surprising since the GPR covers a part of the Pyrenees which is smaller than the central maximum. For this reason the pressure drag, measured along the central transect, will overestimate the North-South drag of the entire ridge. To quantify this overestimation, it is assumed that the pressure drag measured along one given North-South transect located at a given longitude, φ, has the order of magnitude, $NUH^2(\varphi)$. Here H stands for the maximum mountain height at the longitude φ. This predictor of the measured pressure drag was found to perform well along the Greenwich meridian ($\varphi = 0$), according to *Bessemoulin et al* (1993). In this case, an estimation of the North-South component of the stress per unit area of the Pyrenees is,

$$\tau_{reduced} = \frac{1}{\varphi_2 - \varphi_1} \int_{\varphi_1}^{\varphi_2} NUH^2(\varphi) d\varphi \approx \frac{\overline{H^2}}{H^2(0)} D_{measured} \tag{20}$$

later referred to as the reduced measured stress. This ratio between the measured drag and the stress to be parametrized over the GPR can be estimated using the USN dataset, giving the mountain drag per unit area over the GPR as approximately 75% of the drag measured along the PYREX central transect.

Figure 4 shows the comparison between the drag predicted by the SSO scheme with the reduced measured drag, the gravity wave drag contribution to the overall parametrized mountain drag is also shown. The parameters of the scheme are, $C_d = 1$, $G = 0.5$, $F_c = 0.5$, $Ri_c = 1$. This set of parameters was chosen to give a satisfactorily compromise between the forecast performance of the model at T106 and the Pyrex data. Figure 4 shows that in many cases the new scheme gives a drag which is realistic in sign and in amplitude. The maxima and the minima of the measured drag are generally well represented by the scheme. Nevertheless, there are two periods where the scheme is inadequate (Days 27-31 and 54-59). These periods are characterized by strong westerly winds, when the measured drag is mainly a "lift" force, which is not parametrized in the new scheme. Figure 4 also shows that the contribution of the blocked flow drag to the total mountain drag is significant when compared to the gravity wave drag contribution. On many dates (Days 4-6, 7-9, 14.4-15.5, 22-23, 33-35, 38.5-40.5, 43-44, 45-50) the drag contribution from the low level blocked flow significantly enhances the predicted mountain drag, bringing it closer to the measured drag.

The same off-line procedure has been applied to the gravity wave drag scheme previously used (until replaced by this new one), and the results are displayed in Fig 5. It shows that with the constant value, $k = 2.5 \times 10^{-5}$ m^{-1} used (which relates the gravity wave stress amplitude to a typical horizontal wavelength of the orographic

disturbance (*Palmer et al*, 1986), the old scheme gives too small a drag. This would correspond to an overestimation of the typical horizontal wavelength of the disturbance (noted by these authors). Following *Bougeault et al* (1993), multiplying k by 4 i.e. k = 1. x $10^{-4}m^{-1}$, leads to far better agreement with the observations. Nevertheless, even in this configuration, the scheme still shows only a moderate skill. A strong diurnal cycle is present which is unrealistic. This diurnal cycle is a result of using only the three lowest model levels to estimate the incident flow characteristics in the old scheme. Very large amplitude drags occur in the morning when there is large low level stability, and very small amplitude drags in the late afternoon, when the static stability is near neutral.

Figure 6a shows the horizontal momentum flux vertical profiles generated by the new scheme, by the old scheme, and from the measurements for 15 October 1990 at 6UTC (Bougeault, private communication). At low levels, below about 2100 m, the stress profile shows a strong shear which is related to the drag of the blocked flow. Above this layer up to about 4500 m, the stress profile shows a shear related to low level breaking gravity waves. It is important to note that this shear extends significantly above the mountain top, in qualitative agreement with the low level shear stress observed during aeroplane flights between 3900 m and 5700 m. Such an "elevated" low level shear stress does not occur in the old scheme. The vertical stress profile in the new scheme was found to be rather sensitive to the value of the critical Richardson number, Ri_c, as it controls the amount of gravity wave activity that is transmitted to higher levels. At small Ri_c, e.g. around a quarter, most of the wave drag is at high altitudes, and little low level "breaking wave" drag occurs. For $Ri_c=1$, as used in Fig 6, significant low level wave breaking occurs, and the stress decreases with height to a value which fits reasonably with the stress value measured above 6000 m during the aeroplane flights. More profiles are shown in Fig 6b for 16 November 1990 at 6UTC. Here again the new scheme shows strong low level drag contributions from the blocked flow drag and breaking gravity waves. At high levels both the old and new schemes have too large stresses in these particular examples.

5.   VERIFICATION AND DIAGNOSTICS

5.1   On-line verification

Although useful and straightforward to carry out, the preceding calibration does not guarantee that the new scheme will behave properly near the Pyrenees in forecast configurations. In this section, this behaviour is examined at both T106 and T213 resolutions with the ECMWF model. The tests, in which the model orography is a mean orography, will show that the low-level blocked flow drag more than compensates for the envelope orography. Attention is limited to the PYREX Period of Intense Observations (PIO), which covers 25% of the two months of the PYREX campaign, during which the wind component, perpendicular to the mountain range was often large. The procedure followed is close to that presented in *Lott* (1995) where the model transect was as close as possible to the PYREX transect. In the ECMWF model, the

transect is defined along the Greenwich meridian, making its orientation slightly different from that of the PYREX transect which was oriented perpendicularly to the ridge. Although this difference could be handled by suitable interpolation of the data in the model, such a correction was found to have a small impact on the results. These different transects are shown in Fig 7. Since the Pyrenees are quite well represented in the model at T213, the length of the transect in the model was taken a little larger than the Pyrex transect to try to capture, as much as possible, a model pressure drag which can be related to the Pyrenees. As Fig 7 shows, 5 gridpoints along the Greenwich meridian are necessary to define the transect at T213. At T106, the Pyrenees are very difficult to identify, and it is assumed that all the mountain drag has to be parametrized. At this lower truncation, it can be seen that the PYREX transect is almost entirely located between two gridpoints of the model. As a consequence, it will be assumed that the Pyrenees drag in the T106 model is the mean of the sub-grid scale orographic drag between these two gridpoints, with the mountain drag interpreted as the sum of the contribution of the boundary layer turbulence scheme and the sub-grid scale orographic drag. This might seem surprising since the microbarographs were separated by a typical distance of 10 km along the Pyrex transect. However, this network could not capture pressure drag related to turbulence with horizontal scales significantly smaller than this. On the other hand, it is clear that the new scheme and the boundary layer scheme will interact at low levels. Knowledge about turbulence above high and narrow mountains is poor both from a theoretical viewpoint and from measurements and, with such uncertainties, it is reasonable that the total mountain drag (i.e., the model pressure drag + the boundary layer drag + new sub-grid scale orography drag) should be at least as large as the measured pressure drag.

Fig 8 shows the T106 model drag (from forecasts run for 48 hrs with data extracted every 6 hrs) compared to the "reduced" measured drag. The parametrized stress does well during most of the normal ridge configurations. Similar comparison with drags predicted by the forecast model with the old gravity wave drag scheme did not show such skill.

In T213 forecast configurations, the parametrized drags make up the difference between the model pressure drag and the measured pressure drag. With mean orography the model pressure drag is significantly smaller than in the operational model with envelope orography. This is simply related to the fact that with a mean orography, the maximum mountain height of the Pyrenees is significantly smaller than in the operational model with an envelope orography. In fact, *Lott* (1995) has shown that the model drag in the model is well estimated by NVH^2 where V is the wind component perpendicular to the ridge. Since the explicit pressure drag is much reduced in the model with mean orography, the new scheme has to make a substantially larger contribution to the model mountain drag than was the case for the old gravity wave drag when the envelope orography is used. Fig 9 shows that this is the case during all the PYREX POI's. While the old gravity wave drag is very small and does not make up the difference often observed between the model drag and the measured drag, the new orography representation of the sub-grid scale orography gives a parametrized drag

that is large, and makes up in a very consistent way the difference between the model pressure drag and the measured pressure drag.

5.2 Case study

In the new scheme, it is assumed that when the flow component perpendicular to the ridge is large, the mountain drag is mainly related to a slowing down of the low level flow and to upward propagating waves. The amplitude of the wave stress significantly above the mountain top is often small (when compared to the surface stress) because high mountains force large waves which do not really propagate. The large low-level drag can have a significant impact on the flow dynamics at the sub-synoptic scale. The realism of the new scheme can therefore be evaluated by making diagnostics of the low level flow in the model and comparing it to more accurate simulation of the flow near the Pyrenees. One case is examined, using isentropic diagnostics similar to those presented in *Lott* (1995). The impact of the scheme on the flow dynamics is studied by comparing a forecast in which the scheme is active to one in which it is not, with both having mean orography. Fig 10 presents such flow diagnostics on the surface $\theta=293$ K. At this level, the synoptic flow is essentially from the north-west (Fig 10a). Over the mountains, it is significantly deflected southward, and in the lee of the ridge the wind is significantly decelerated. Fig 10b shows the elevation of this isentropic surface, ranging from about 1700 m above the model ground upstream of the mountain and descending to 1100 m south of the mountain. Although significantly distorted, this layer is at an altitude which experiences the low-level drag in the new scheme. The impression that the flow is decelerated at this level is reinforced by the presence of a vorticity dipole which begins over the mountain and extends significantly downstream (Fig 10c). Nevertheless, the presence of such a dipole can be due to a conversion of planetary vorticity into relative vorticity by changes in the isentropic layer depth, while conserving potential vorticity. In this case the occurrence of the vorticity dipole would essentially depend on reversible processes related to the advection by the flow of the potential vorticity. To evaluate if this reversible picture applies here, Fig 10d shows the Bernoulli function,

$$B = C_p T + gz + \frac{u^2 + v^2}{2} \tag{21}$$

which is a conserved quantity on isentropic surfaces (*Schär*, 1993) in the absence of body forces and diabatic heating. The Bernoulli function shows a deficit across the ridge, since the flow essentially crosses the Bernoulli "contours" as it passes over the ridge. To verify that this deficit is related to the new scheme, Figs 10e and 10f shows the flux of absolute vorticity (*Haynes and McIntyre*, 1987), and the contribution to this flux from the non-conservative body forces and diabatic heating which are determined by the physical parametrization scheme of the model, i.e.

$$\vec{u}\,(\xi_{r\theta} + f) + \vec{k} \times \vec{F} - \vec{k} \times \dot{\theta}\frac{\partial \vec{u}}{\partial \theta} \tag{22}$$

where $\vec{u}$ and $\xi_{r\theta}$ are the isentropic wind and the isentropic relative vorticity respectively, f is the planetary vorticity, $\vec{F}$ and $\dot{\theta}$ represent the body force and the diabatic processes related to the parametrization schemes, respectively. Comparing Figs 10e and 10f, the non-advective contribution to the absolute vorticity flux is clearly large over the mountain. Likewise comparing Fig 10e with the Bernoulli function map, the deficit of the Bernoulli function (which is the stream function of the absolute vorticity flux (*Schär*, 1993)) must be due to the parametrized processes. The fact that the new scheme plays a predominant role in the production of the wake is further confirmed looking at the non-conservative forcing when the new scheme is switched off. This is significantly smaller (Fig 11b), and the vorticity dipole is less pronounced (Fig 11a). *Lott* (1995) has shown similar isentropic diagnostics of the mesoscale re-analysis of the PYREX data from the Peridot model (*Bougeault and Mercusot*, 1992). In these diagnostics, a very similar wake was observed at this isentropic level, due to flow separation processes occurring on the Pyrenees flanks.

6.   TESTING OF THE FORECAST PERFORMANCE

The preceding sections are intended to show that the new scheme is well based dynamically, and that it corresponds well with PYREX data diagnostics. However, a parametrization scheme in a global numerical model must perform well under a much wider range of situations. Furthermore, the ECMWF model is routinely run at several horizontal resolutions ranging from T63 to T213. Consequently, extensive testing is required in such a model before a new parametrization scheme can be considered suitable to replace a previous one. Since different horizontal resolutions imply different basic orographies and different associated sub-grid scale orographic fields, the resolution issues are particularly prominent. In view of the PYREX testing at T106 and T213, and the fact that the current ECMWF operational system is run at T213, most of the forecast testing has been done at these higher resolutions. Results from T63 forecasts and longer simulations will not be discussed here. As has been discussed already, the new scheme is designed to be used together with a <u>mean</u> orography.

6.1   An 'effective' orography

Since an envelope orography is substantially higher than the mean one to be used with the new SSO scheme proposed here, the question arises as to whether there is an 'effective' orography implied when using the new scheme since it influences the flow well above the mean orographic heights. As presented here, the scheme only directly affects the momentum and not temperature or moisture variables. As such, the 'effective' orography for surface fluxes of heat and moisture, for example, is the (resolved) mean one. However, there is also an effect on these fluxes through the near-surface wind field which will be modified by the new scheme; this is, however, difficult to quantify. For the momentum there is the obvious impact of Z_b, the blocking height, but since the sub-grid scale orography also has a vertical profile (given by the square root part of Eq 16), a possible better measure of 'effective' orography ought to be given by

$$h_{eff}(x,y) = h_{mean}(x,y) + \delta h(x,y,t) \text{ where } \delta h(x,y,t) = \int_0^{z_b} \sqrt{\frac{Z_b - z}{\mu + z}} dz$$

the integral being a function of both location and time. This integral can be evaluated analytically giving

$$\delta h = z_b((\beta^2 + 1)Tan^{-1}(1/\beta) - \beta)$$

where $\beta^2 = \mu/Z_b$. For $Z_b = \mu$, for example, $\delta h \sim 0.57\mu$.

Fig 12 shows an example of this orographic field computed as a ten-day forecast average. Also shown is the corresponding mean orography. This 'effective' orography increment can be large (over a thousand metres for most major mountain ranges) and thus provides a higher 'effective' orography than a one standard deviation envelope would.

6.2 Forecasts without reassimilation

One of the ways that the impact of the parametrization scheme can be assessed is using objective skill scores. Ideally forecasts should be run from analyses generated with an assimilation system using the same model as the forecast one (see section 6.3), however to obtain a broad annual spread of initial dates, the scheme was first tested without reassimilation. Fig 13 shows comparisons of two sets of twelve forecasts (one per calendar month) run at T106 and T213 as measured by rms height errors. The comparison is between forecasts run with mean orography only and with mean orography plus the new scheme. In general the impact of the scheme is positive. This is also true for tropical wind verification (not shown). There is, however, little impact for the S Hemisphere.

6.3 Forecasts including reassimilation

Four periods of assimilation and forecasts were carried out. For each period the comparison was made with a forecast system that used envelope orography and the old GWD scheme. The data assimilation system is sensitive to the orography and since the use of near-surface data and especially radiosonde data depends on the observing station heights. Consequently more data is used when the assimilating model uses mean orography. Three T106L31 experiments for two-week periods in January, April and August, and a two-week T213L31 experiment for March 1994 were run. The mean results for the three lower-resolution periods are similar to those of section 6.2, with a positive impact in January (Fig 14a) and a near neutral one in August (not shown). The T213 (March) results are also slightly positive (Fig 14b). There is a modest positive impact in the S Hemisphere probably due to the use of mean orography in the data assimilation.

Prior to operational implementation of this scheme, two three-week T213 assimilation and forecast experiments were carried out. For one, the period 6 Dec 1994-26 Dec 1994, the forecasts (only) were rerun

with the orography scheme switched off i.e. with mean orography only. This isolates the impact of the new scheme on the forecast model only. Fig 15 shows the rms 500 mb height errors averaged over the set of nineteen forecasts (8/12/94-26/12/94) and the benefits of the new scheme are clear.

7.   CONCLUDING REMARKS

A new parametrization of sub-grid scale orographic drag has been presented. It encompasses recent developments in the nonlinear theory of stratified flows around obstacles. In this scheme, particular attention has been paid to the drag in the model layers of the atmosphere below the sub-grid scale mountain peaks. This low level part of the scheme replaces the envelope enhancement of model orography. The upper part of the scheme still represents the role of gravity waves. This part has been revised to allow a better representation of mountain ridge orientation and anisotropy. It also removes some arbitrary assumptions in the previous scheme. The depth over which the gravity wave drag part of the scheme is felt by the flow at low levels is now linked to dynamical properties of the mountain waves. The incident wind characteristics are calculated above the boundary layer (when the mountain is high enough) suppressing the strong diurnal cycle which was found to occur in the old gravity wave drag scheme. The parameters of the new scheme have been calibrated using an off line procedure, in which the scheme has been used to predict the mountain drag measured during PYREX. In this calibration, the new drag scheme outperforms the old gravity wave drag scheme, and fits well with the surface drag measured during field experiments. It also gives more realistic momentum flux vertical profiles than those of the old scheme. It was further shown that the new scheme has a realistic dynamical impact on the model dynamics in the vicinity of mountains, reinforcing the scheme's basic premise that mesoscale mountain drag slows down the low-level flow under most atmospheric situations. Results from forecast experimentation such as skill scores, precipitation amounts and distribution indicate that overall the combination of mean orography together with the new scheme performed better than that using envelope orography plus the current GWD scheme. As was noted in section 4, there remains the problem of representing the lateral force present when there is strong flow parallel to the ridges. This is the subject of ongoing work. The scheme is beneficial to the forecast skill of the ECMWF model at all forecast ranges and has been in operational use since 4 April 1995. The theoretical background to this work suggests that not only models of climate and GCM resolution but also much higher resolution limited area models should parametrize the drag due to the 'blocked' flow.

REFERENCES:

Baines, P G and T N Palmer, 1990: Rationale for a new physically-based parametrization of sub-grid scale orographic effects. ECMWF Technical Memorandum 169.

Bessemoulin, P, P Bougeault, A Genoves, A Jansa Clar and D Puech, 1993: Mountain pressure drag during PYREX. Beitr Phys Atmosph, 66, 305-325.

Boer, G J, N A Mc Farlane, R Laprise, J D Henderson and J P Blanchet, 1984: The Canadian Climate Centre spectral atmospheric general circulation model. Atmos-Ocean, 22, 397-429.

Bougeault, P, A Jansa, J L Attie, I Beau, B Benech, B Benoit, P Bessemoulin, J L Caccia, J Campins, B Carrissimo, J L Champeaux, M Crochet, A Druilhet, P Durand, A Elkhalfi, P Flamant, A Genoves, M Georgelin, K P Hoinka, V Klaus, E Koffi, V Kotroni, C Mazaudier, J Pelon, M Petitdidier, Y Pointin, D Puech, E Richard, T Satomura, J Stein and D Tannhauser, 1993: The atmospheric momentum budget over a major mountain range: first results of the PYREX field program. Ann Geophysicae, 11, 395-418.

Bougeault, P and C Mercusot, 1992: Atlas des réanalyses PERIDOT de l'expérience PYREX. Note de travail N°8 du groupe de météorologie à moyenne echelle. CNRM, F-31057 Toulouse, France.

Clark, T L and M J Miller, 1991: Pressure drag and momentum fluxes due to the Alps. II Representation in large-scale atmospheric models. Q J Roy Meteor Soc, 117, 527-552.

Etling, D, 1989: On atmospheric vortex street in the wake of large islands. Meteorol Atmos Phys, 41, 157-164.

Gurevich, M I, 1965: Theory of jets in ideal fluids. Academic Press.

Haynes, P H and M E McIntyre, 1987: On the evolution of vorticity and potential vorticity in the presence of diabatic heating and frictional or other forces. J Atmos Sci, 44, 828-841.

Kirchoff, G, 1876: Vorlesungen über mathematische physik. Leipzig 1876.

Lamb, H, 1932: Hydrodynamics. University Press.

Landweber, L, 1961: Motion of Immersed and Floating Bodies. Handbook of Fluid Dynamics. 1st Edition. Mc Graw-Hill.

Lott, F, 1995: Comparison between the orographic response of the ECMWF model and the PYREX 1990 data. To appear in Quart J Roy Met Soc.

Miles, J W and H E Huppert, 1969: Lee waves in a stratified flow. Part 4: Perturbation approximations. J Fluid Mech, 35, 497-525.

Miller, M J, T N Palmer and R Swinbank, 1989: Parametrization and influence of sub-grid scale orography in general circulation and numerical weather prediction models. Meteor & Atmos Phys, 40, 84-109.

Miranda, P M A and I N James, 1992: Non-linear three-dimensional effects on gravity waves: splitting flow and breaking waves. Quart J Roy Met Soc, 118, 1057-1081.

Palmer, T N, G J Shutts and R Swinbank, 1986: Alleviation of systematic westerly bias in general circulation and numerical weather prediction models through an orographic gravity wave drag parametrization. Quart J Roy Met Soc, 112, 2056-2066.

Phillips, S P, 1984: Analytical surface pressure and drag for linear hydrostatic flow over three-dimensional elliptical mountains. J Atmos Sci, 41, 1073-1084.

Schär, C, 1993: A generalization of Bernoulli's theorem. J Atmos Sci, 50, 1437-1443.

Smith, R B, 1979a: Some aspects of the quasi-geostrophic flow over mountain. J Atmos Sci, 36, 2385-2393.

Smith, R B, 1989: Mountain induced stagnation points in hydrostatic flows. Tellus, 41a, 270-274.

Stein, J, 1992: Investigation of the regime diagram of hydrostatic flow over a mountain with a primitive equation model. Part 1: two-dimensional flows. Monthly Weather Review, 120, 2962-2976.

Tibaldi, S, 1986: Envelope orography and maintenance of quasi-stationary waves in the ECMWF model. Adv Geophys, 29, 339-374.

Wallace, J M, S Tibaldi and A Simmons, 1983: Reduction of systematic forecast errors in the ECMWF model through the introduction of an envelope orography. Quart J Roy Met Soc, 109, 683-717.
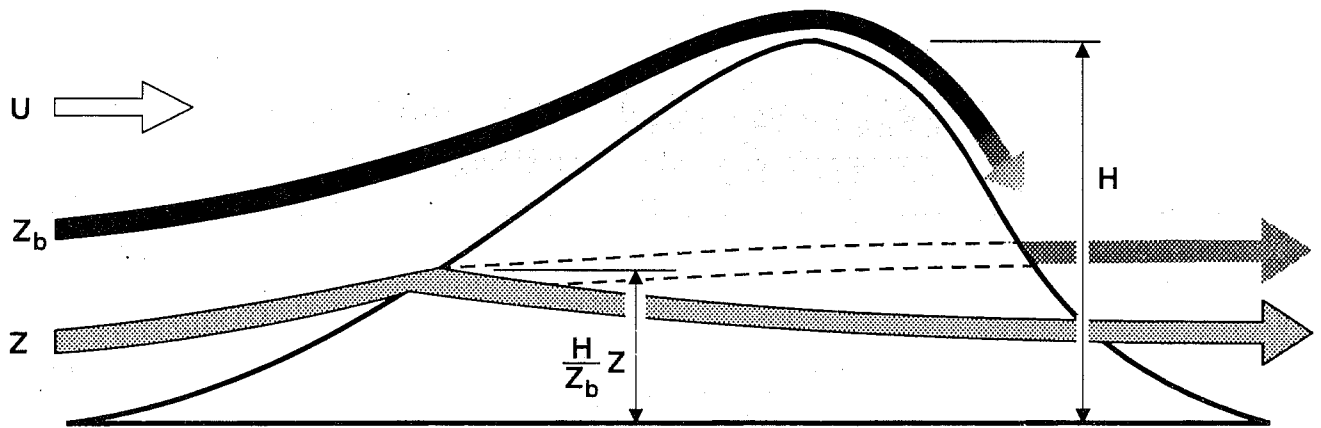
Fig 1   Schematic representation of the low level flow behaviour parametrized in the new-scheme (see text for details).
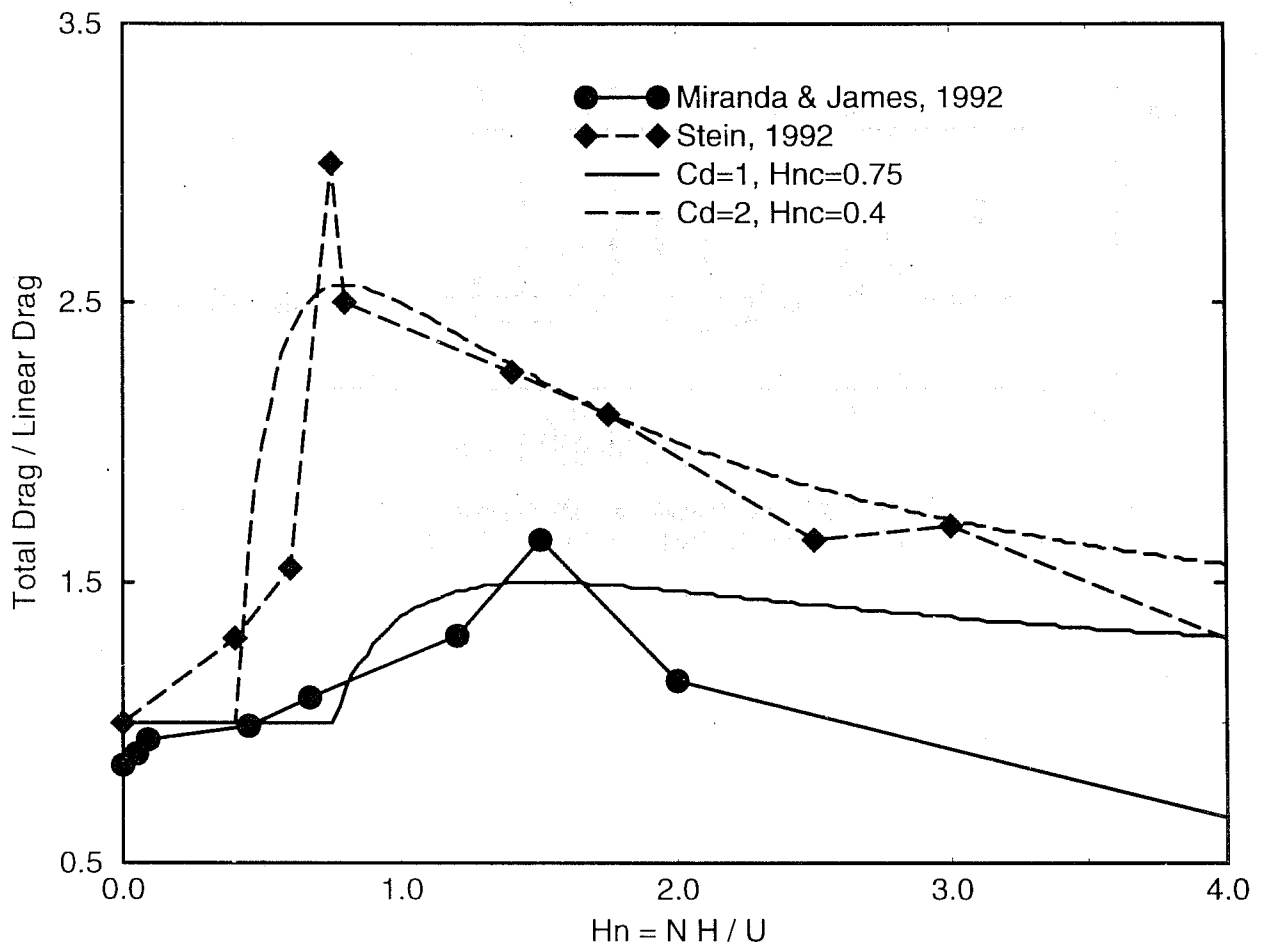
Fig 2   Ratio between the total mountain drag and the linear gravity wave drag as a function of H_N. The continuous line and the dotted line correspond to the drag ratio predicted by the conceptual model upon which the new SSOD scheme is based. The dotted line with diamond symbols corresponds to values found in 2D nonlinear simulations (*Stein*, 1989). The continuous line with circle symbols correspond to values found in 3D nonlinear simulations (*Miranda and James*, 1992).

19
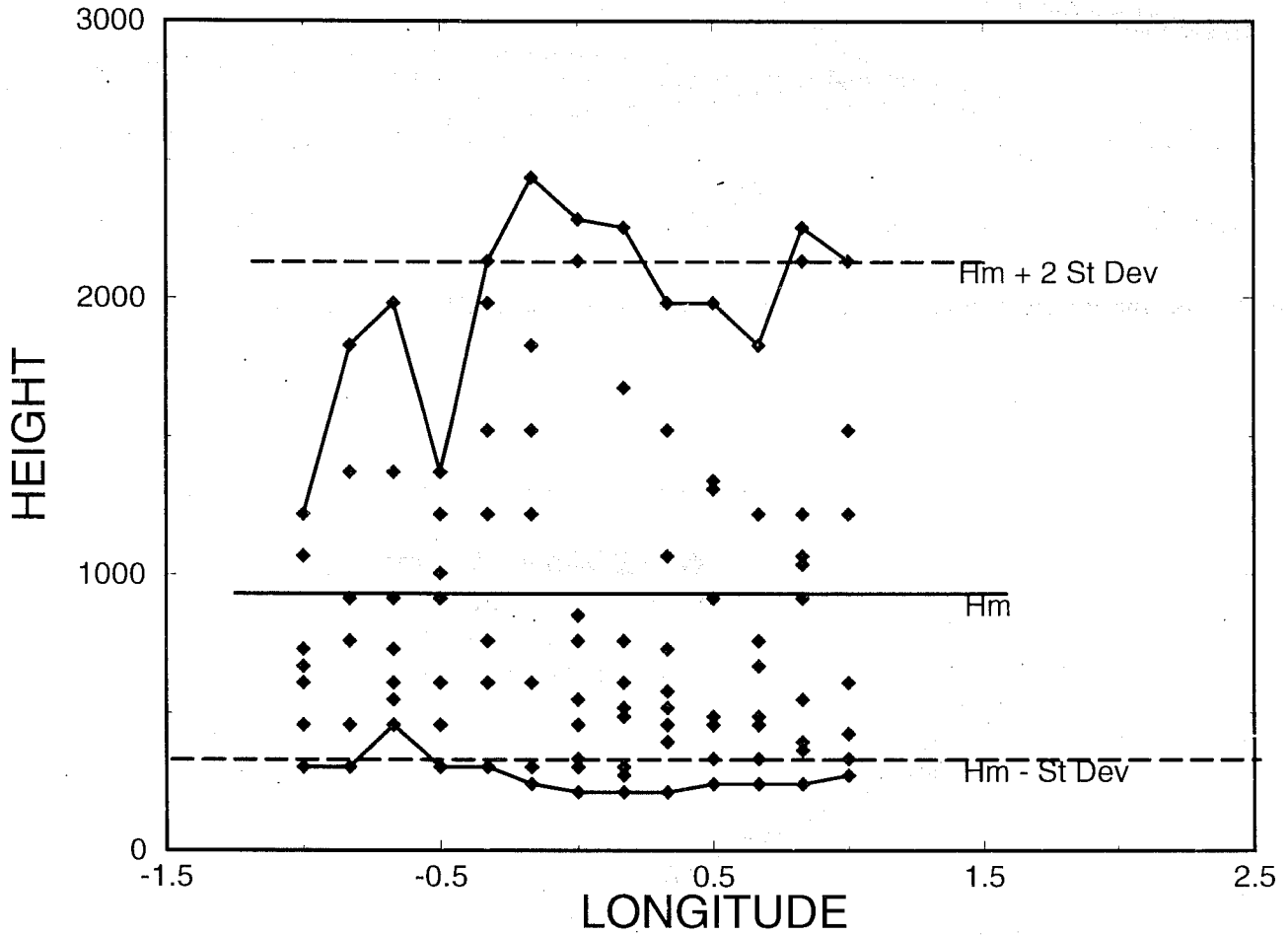
Fig 3   The USN orography dataset (10'x10') of mountain elevations plotted as a function of longitude for a grid point region covering the Pyrenees mountain range [(-1W,1E)x(41.7N,43.3N)].

Estimation of the mountain drag over the Pyrenees.
New Subgrid Scale Orographic Drag
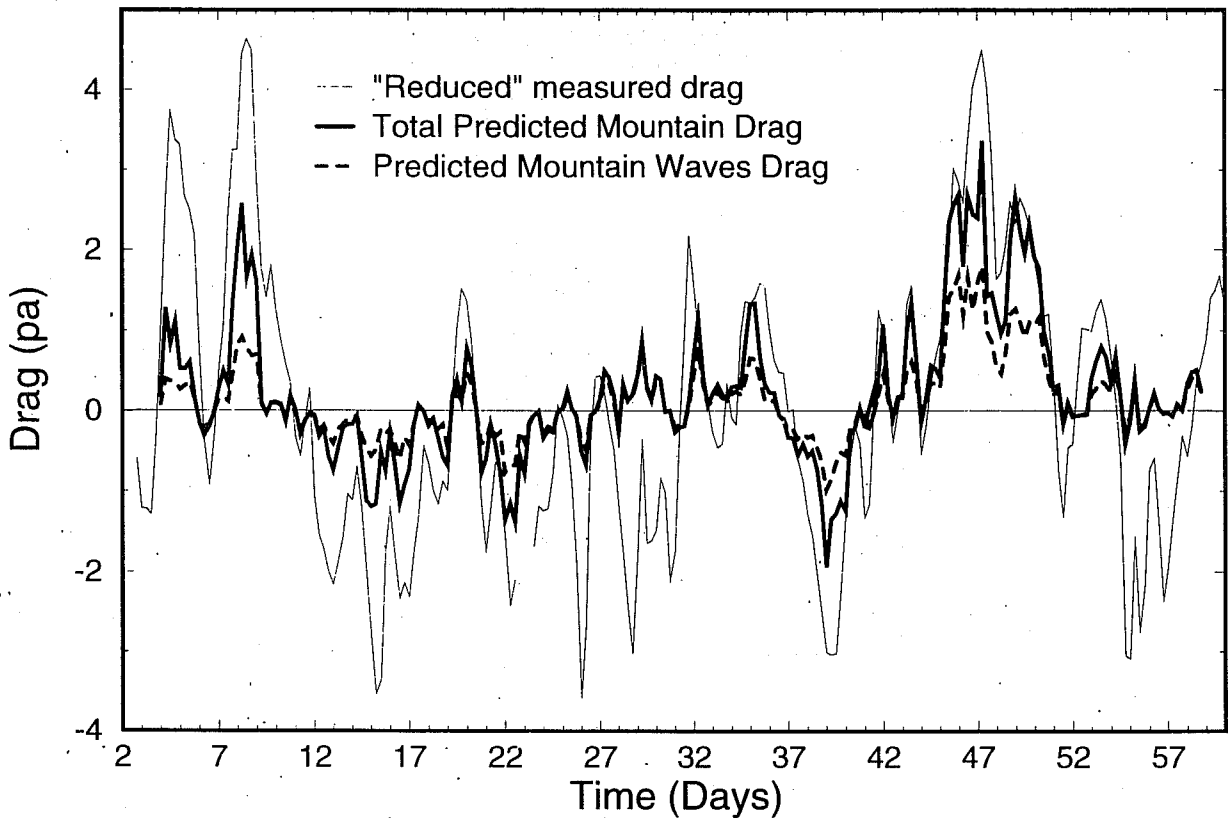
Fig 4   Off-line calibration: comparison between the pressure drag measured during the PYREX field experiment, and the drag predicted by the new scheme.

Estimation of the mountain drag over the Pyrenees.
Old Gravity Wave Drag Scheme
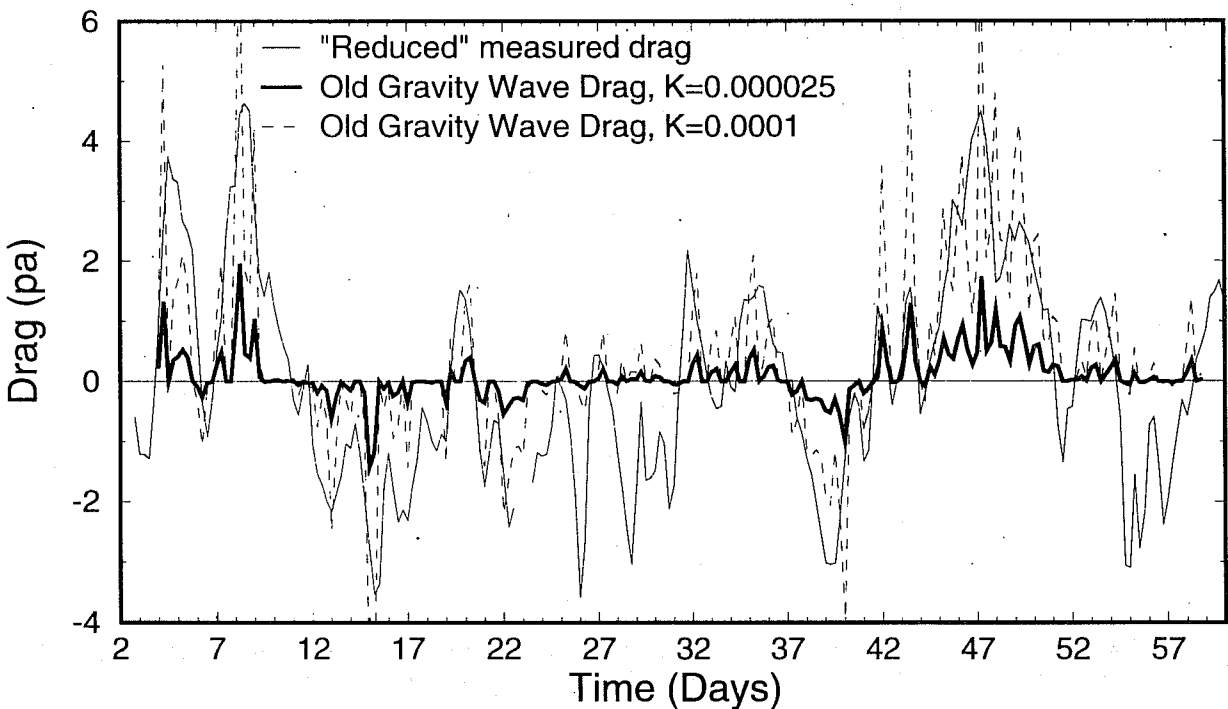
Fig 5   Same as Fig 4 but for the old gravity wave drag scheme. The dashed line (k=0.000025 m⁻¹) shows the operational gravity wave drag scheme. The dotted line (k=0.0001 m⁻¹) show the same operational scheme but for a larger value of the constant k.
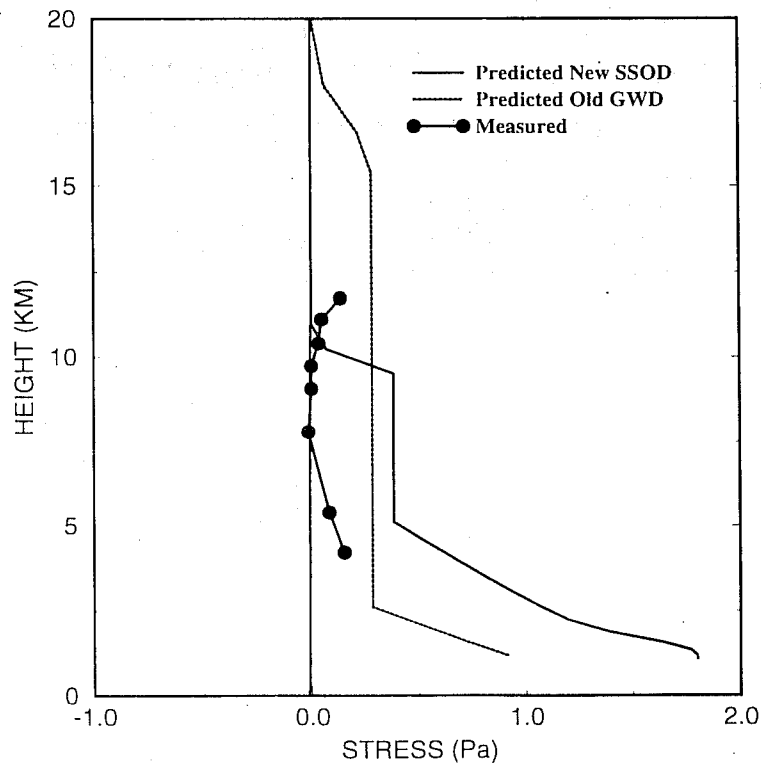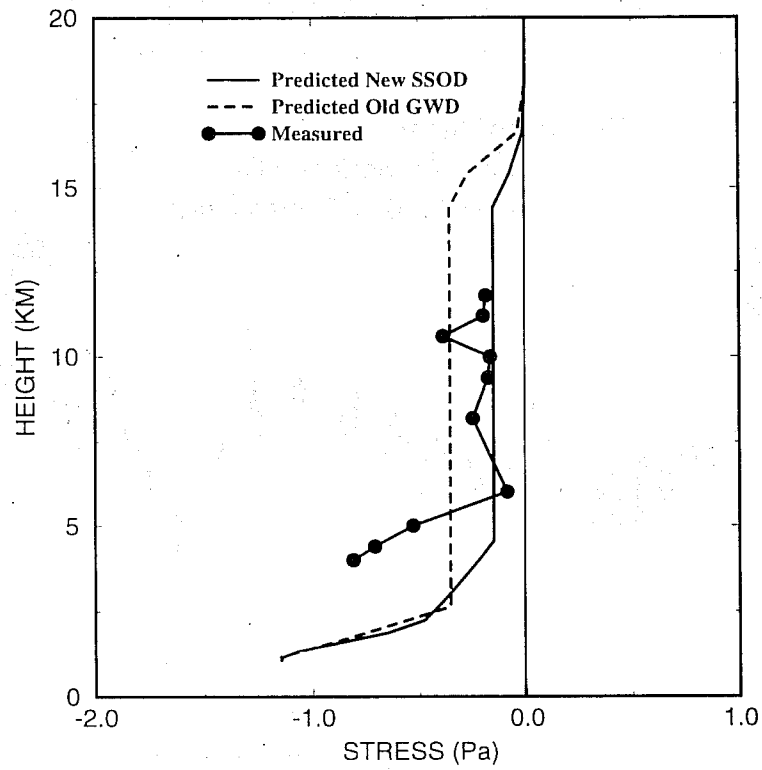
Fig 6   Off-line calibration: stress vertical profiles predicted by the new scheme, by the old gravity wave drag scheme and as measured. (a) 15 October 1990, 6 UTC. (b) 16 November 1990, 6 UTC.
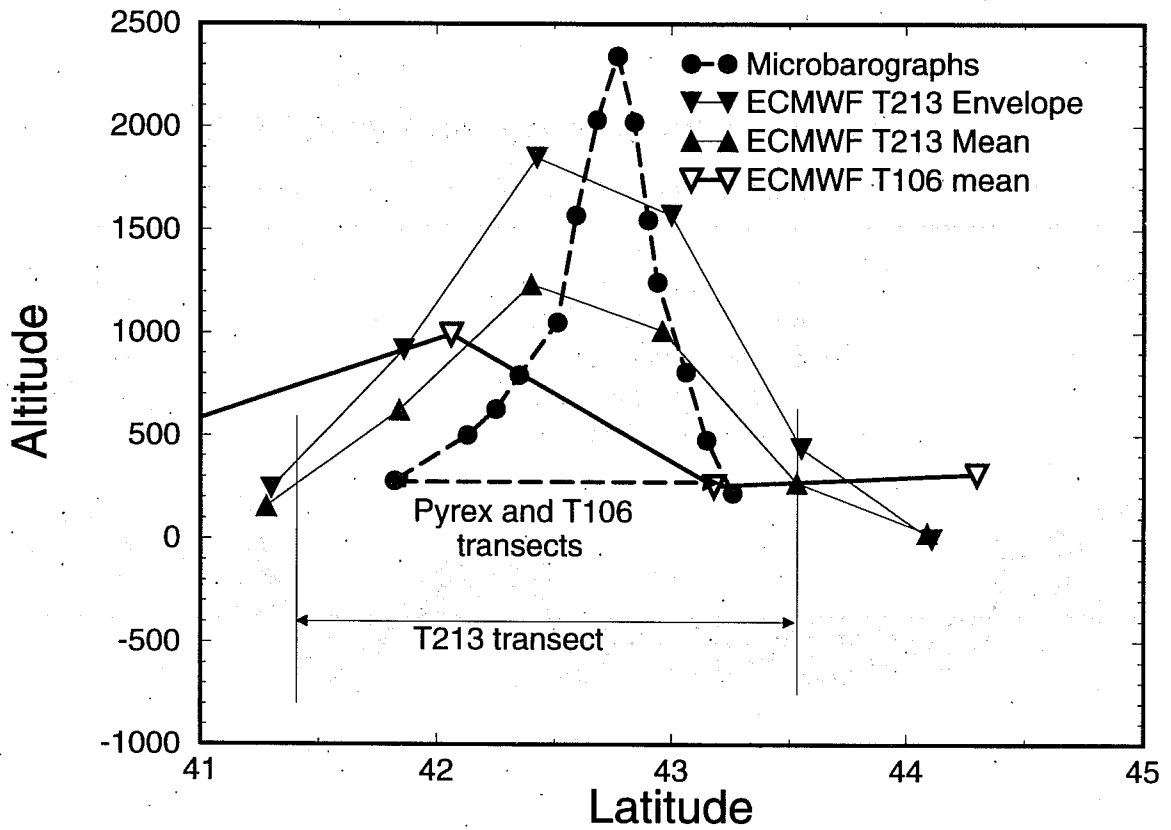
Fig 7 Orography profiles of the transects along which the pressure drags are calculated.

T106 model drag during Pyrex POI's

New Subgrid Scale Orography + mean orography
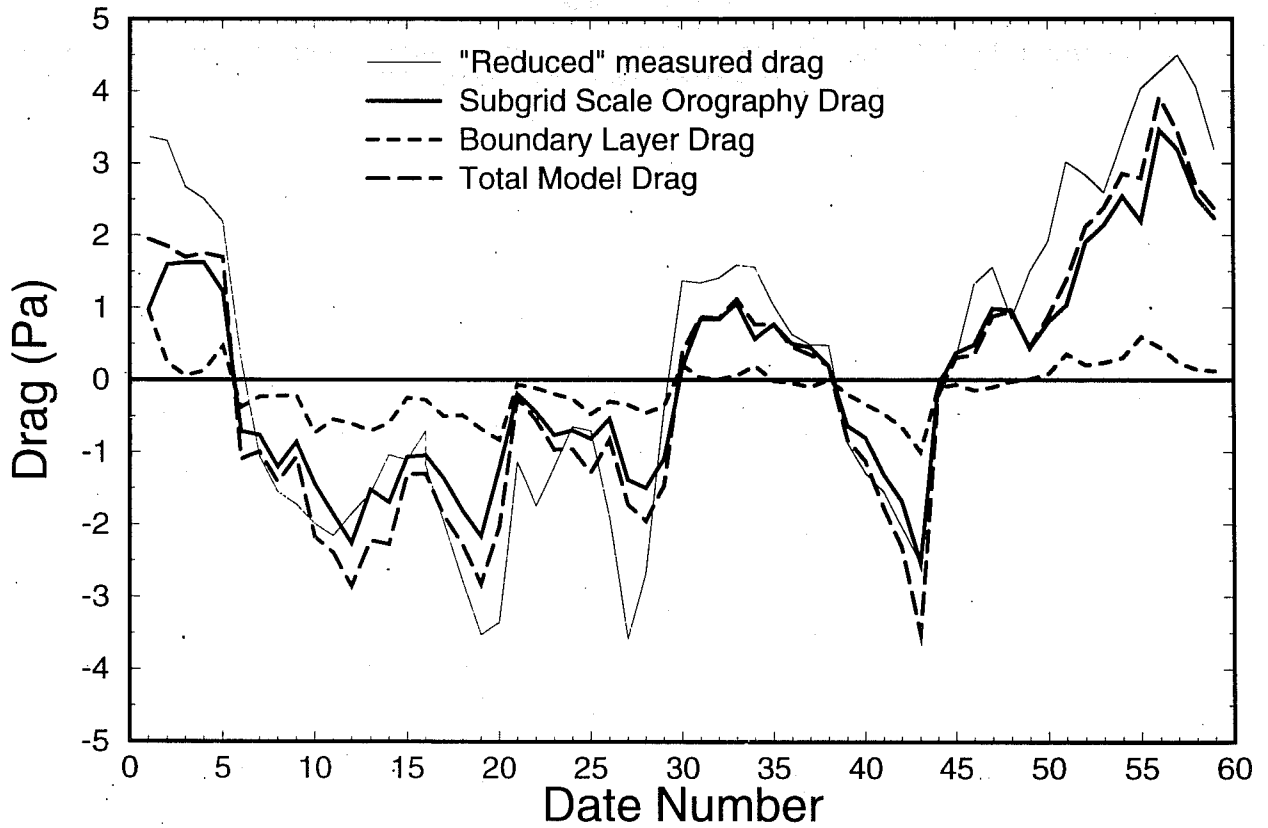
Fig 8 T106 forecasts, ECMWF model with mean orography and the new sub-grid scale orographic drag scheme. Parametrized mountain drags during PYREX.

T213 model drag during Pyrex POI's

New Subgrid Scale Orography + mean orography
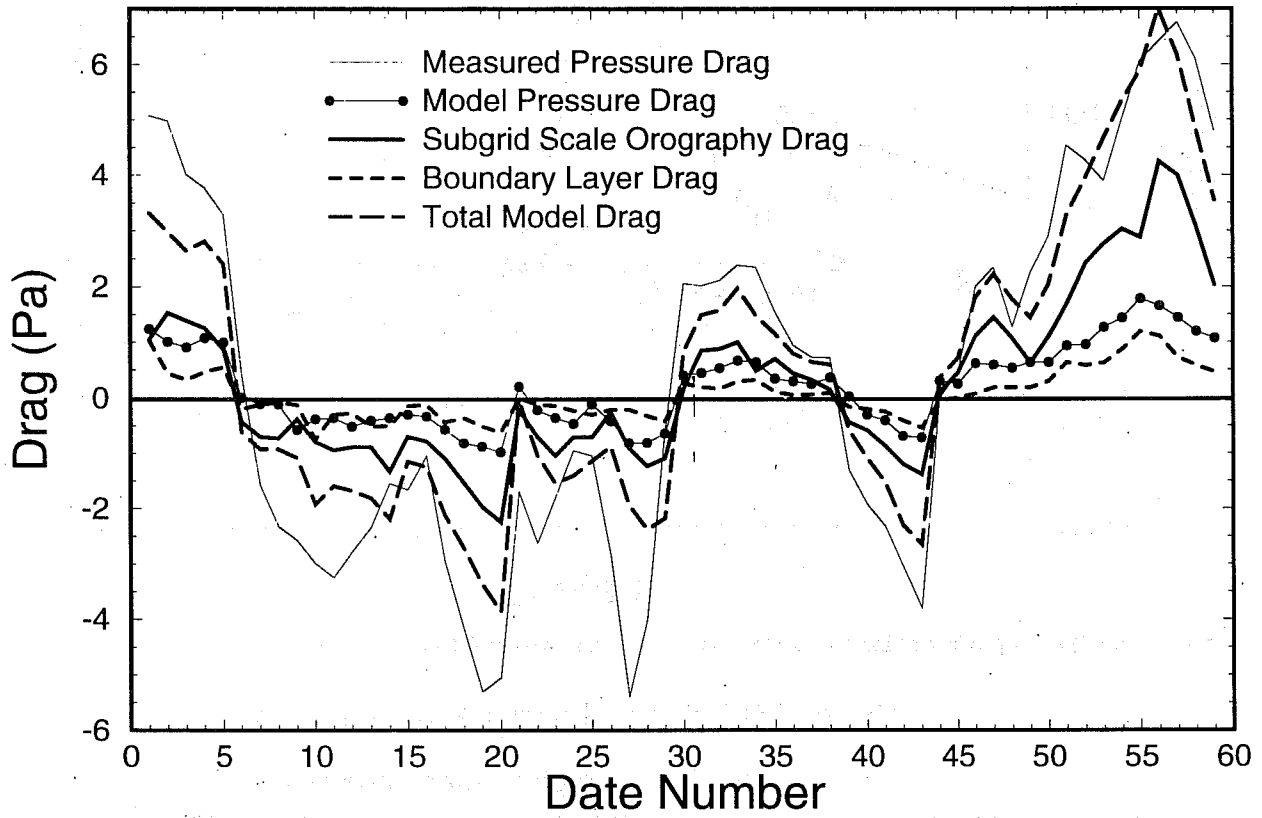
Fig 9   T213 forecasts, ECMWF model with mean orography and the new sub-grid scale orographic drag scheme. Explicit model pressure drag and parametrized mountain drags during PYREX.
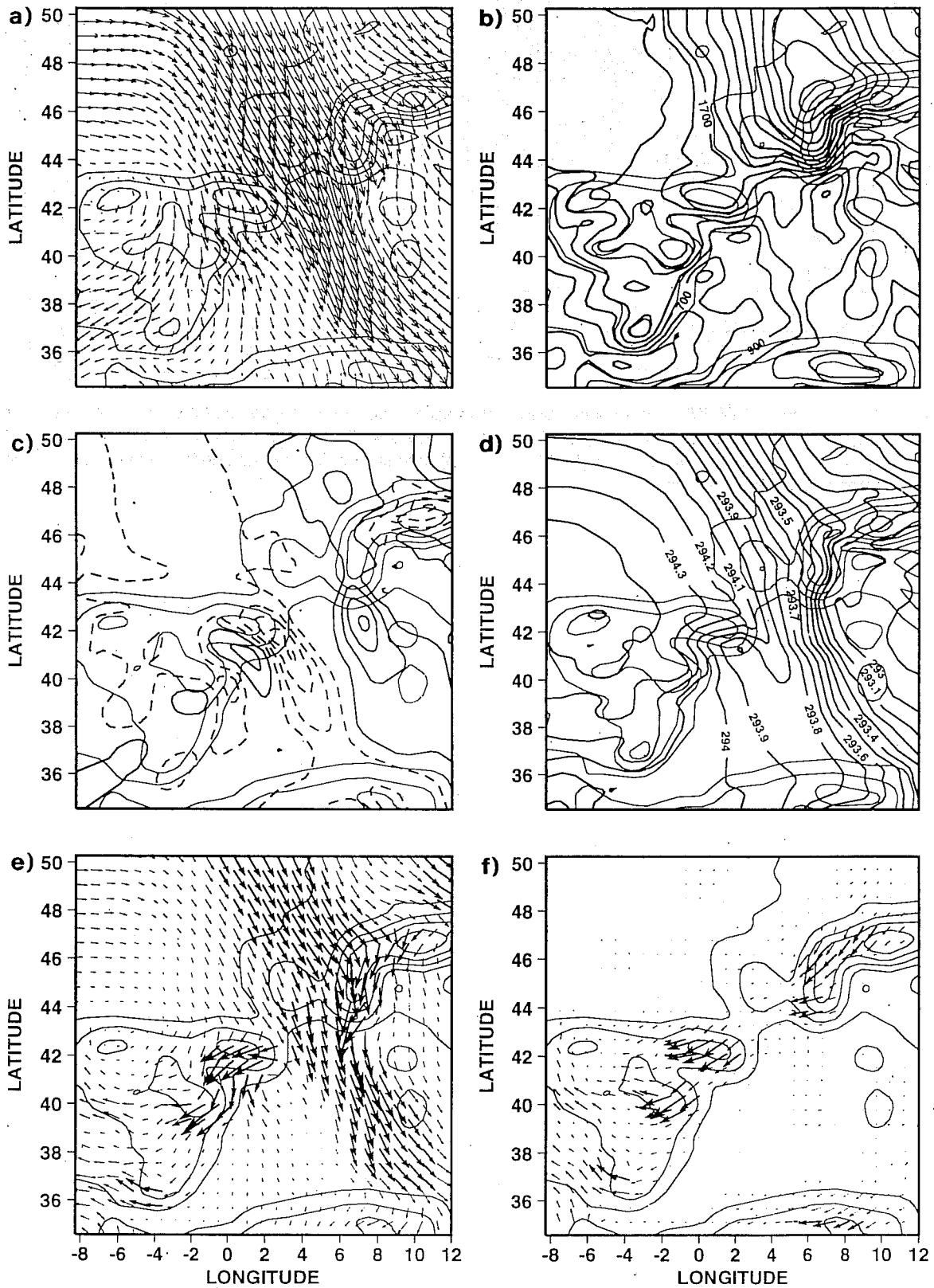
Fig 10   T213 forecast, ECMWF model with mean orography and the new sub-grid scale orographic drag scheme. 15 November 1990 at 6 UTC.   Orography (interval=400 m) and flow diagnostics on the isentropic surface Θ=293 K. (a) wind; (b) height of isentropic surface, interval=200 m; (c) isentropic relative vorticity, interval= 0.5 10^{-4} s^{-1}; (d) Bernoulli function, interval= 100 J kg^{-1}; (e) total potential vorticity flux; (f) potential vorticity fluxes due to the parametrized frictional forces and diabatic heating.
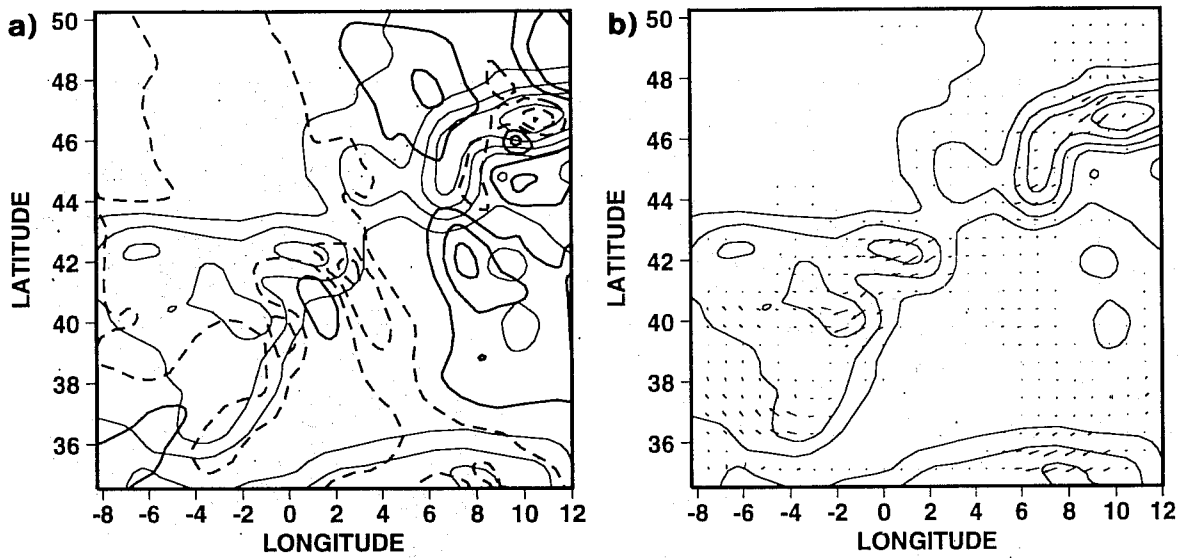
Fig 11   T213 forecast, ECMWF model with mean orography and no sub-grid scale orographic drag scheme. 15 November 1990 at 6 H. Orography (C.I.=400 m) and flow diagnostics on the isentropic surface Θ=293 K. (a) isentropic relative vorticity, interval= $0.5 \ 10^{-4} \ s^{-1}$; (b) potential vorticity fluxes due to the parametrized frictional forces and diabatic heating.
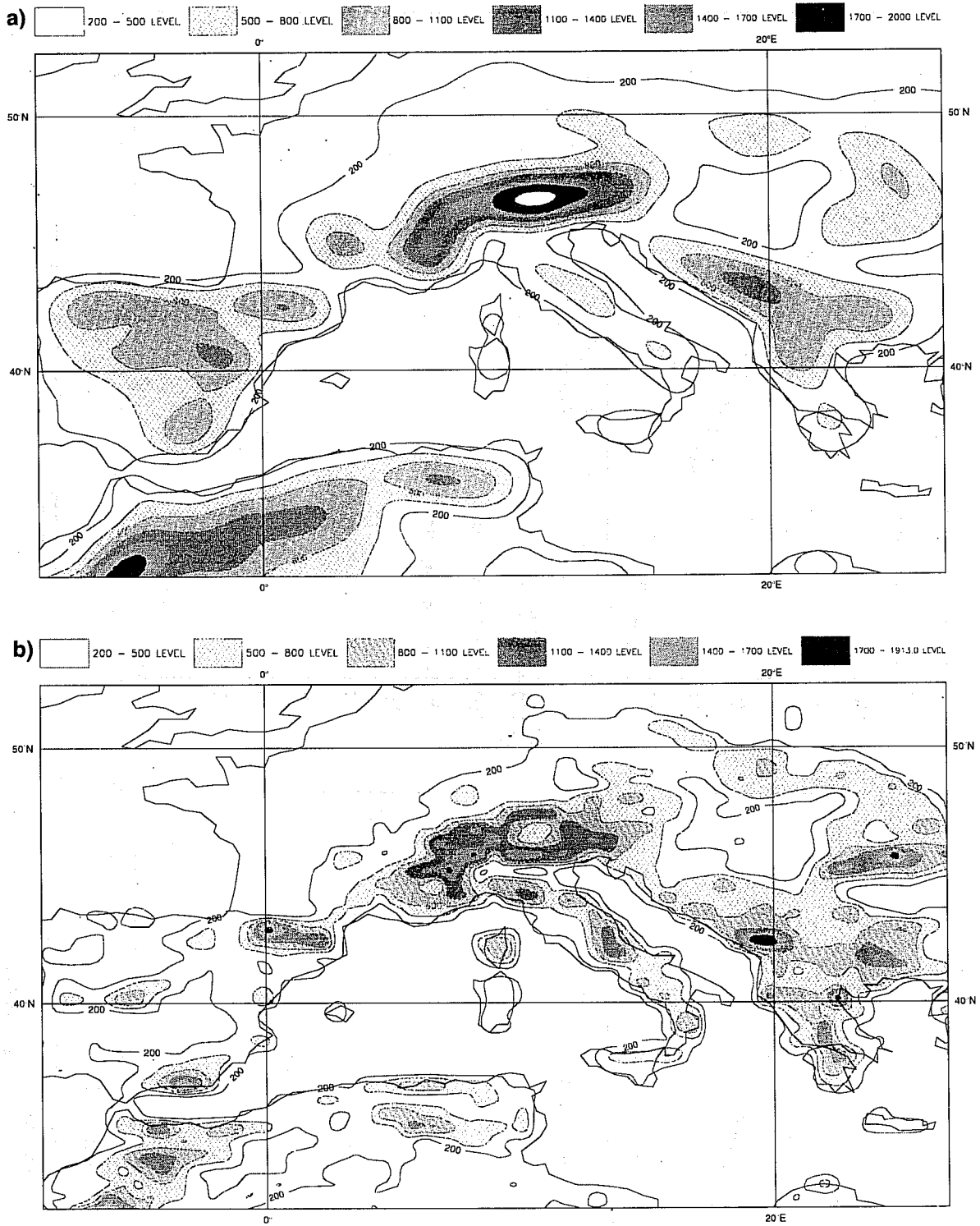
Fig 12   a) The T213 orography, shading every 300 m.
b) The T213 'effective' orography enhancement computed from a 10-day forecast mean (initial date 15 Jan 1995).
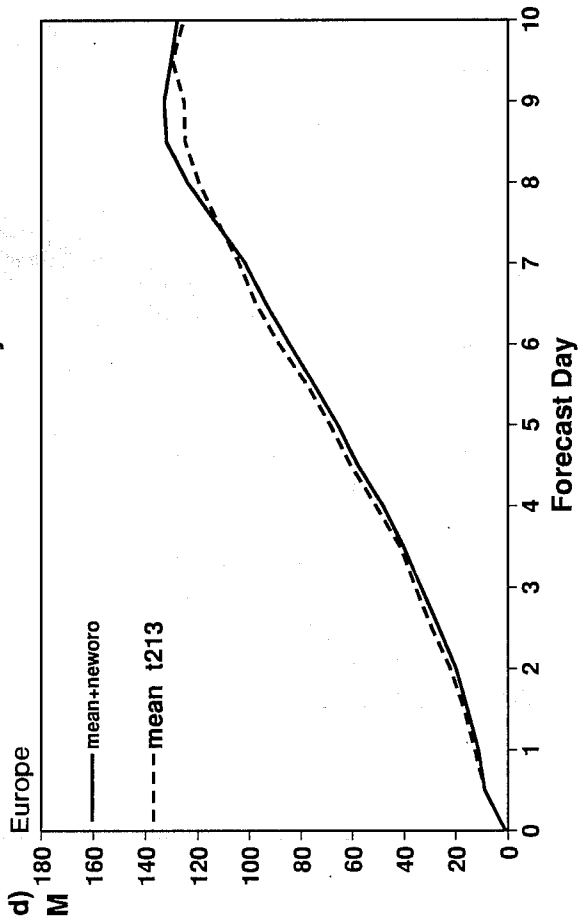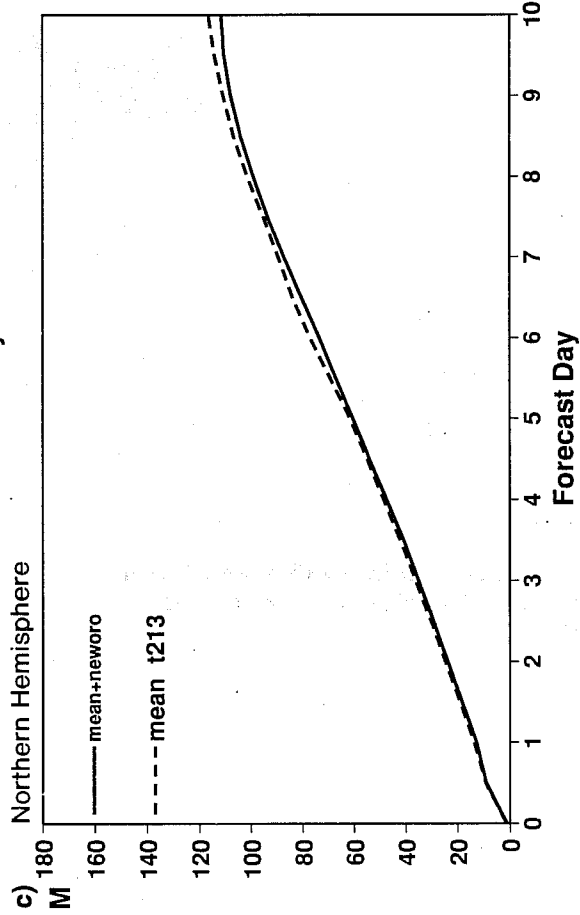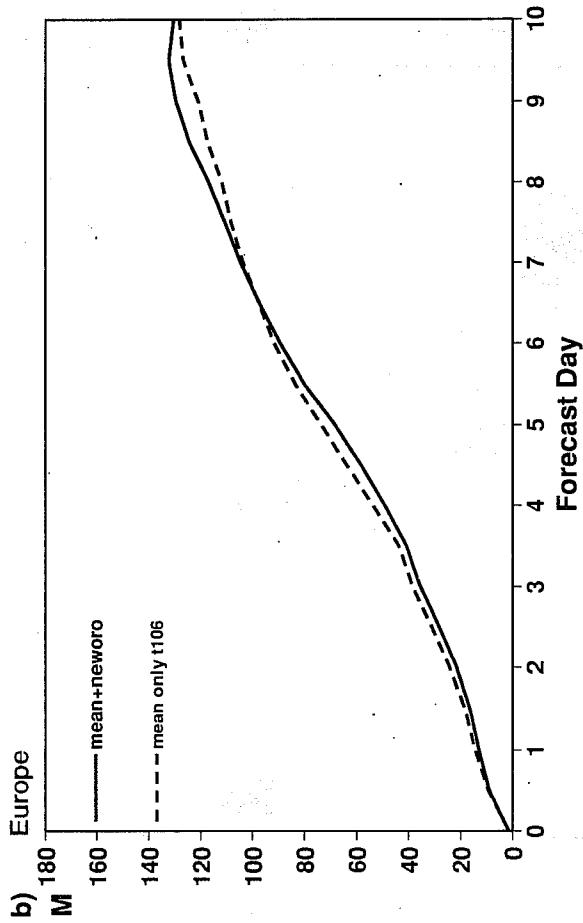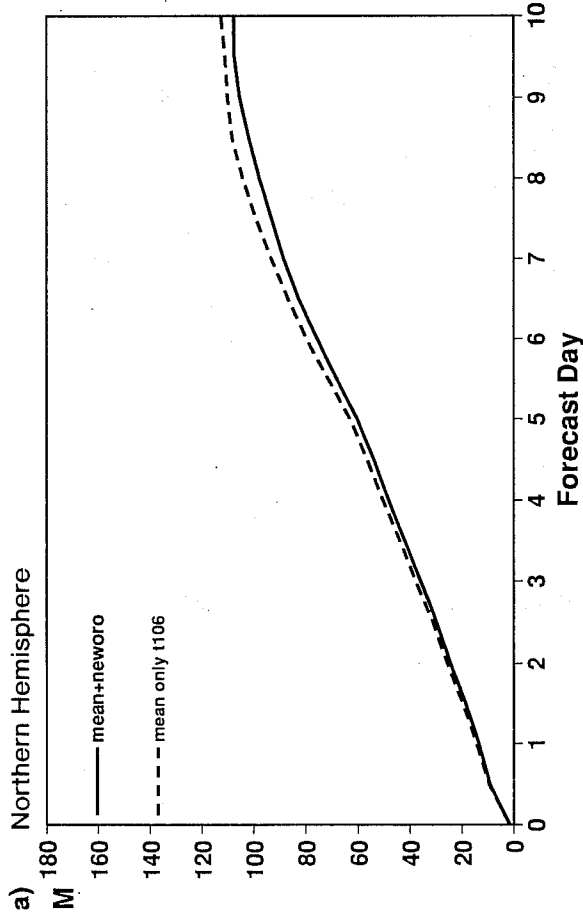
Fig 13   500 mb rms height errors for two sets of 12 T106 forecasts (with mean orography) with and without the new
scheme
a) N Hemisphere, b) Europe
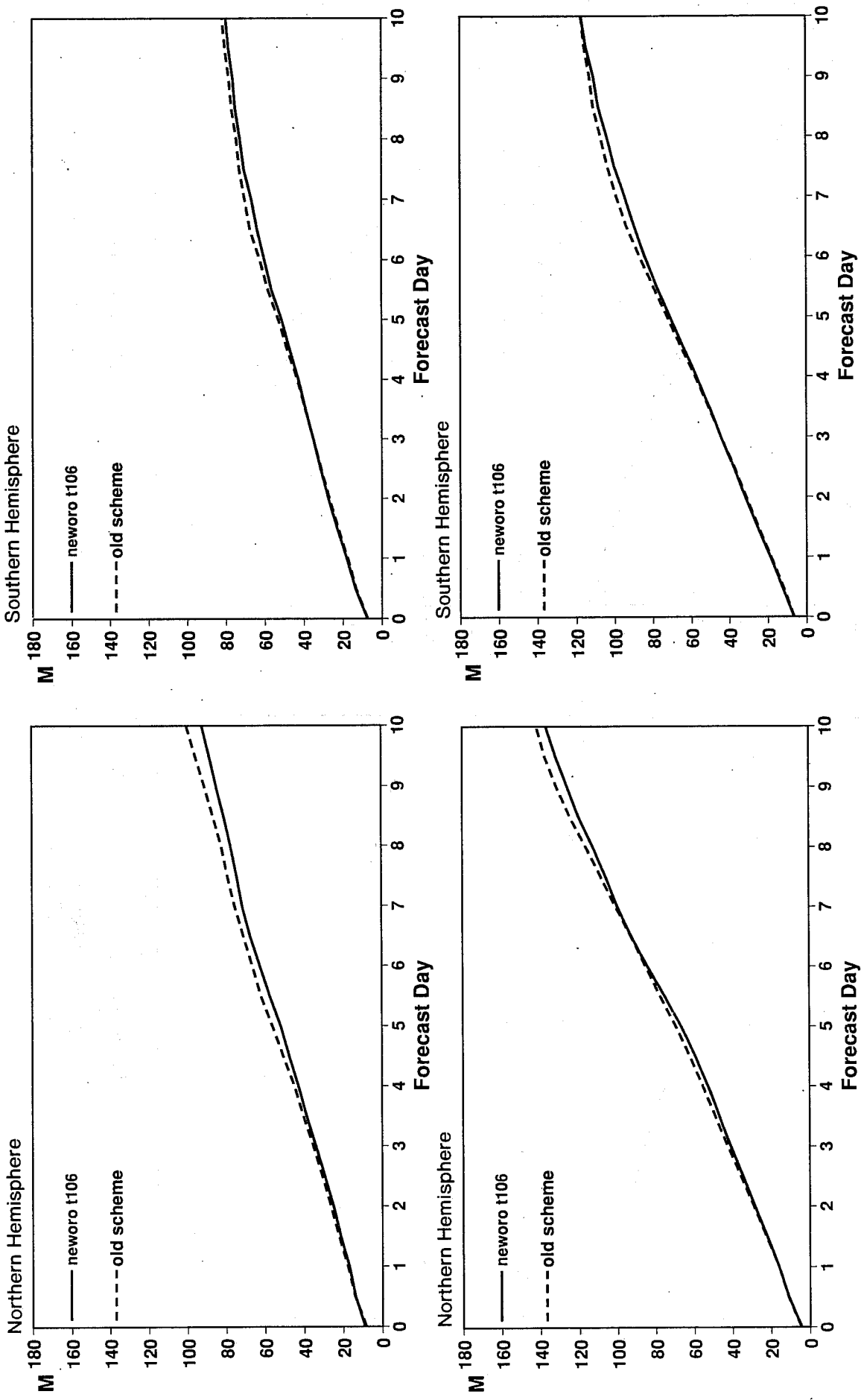c) and d) As a) and b) but for T213 resolution.

28

Fig 14a 1000 mb (upper) and 500 mb (lower) rms height scores for fourteen consecutive forecasts (initial dates 94/01/02-94/01/15). Left column - N Hemisphere, right column - S Hemisphere. Forecasts and assimilation with T106 system. New scheme, solid lines; old scheme, dashed lines.
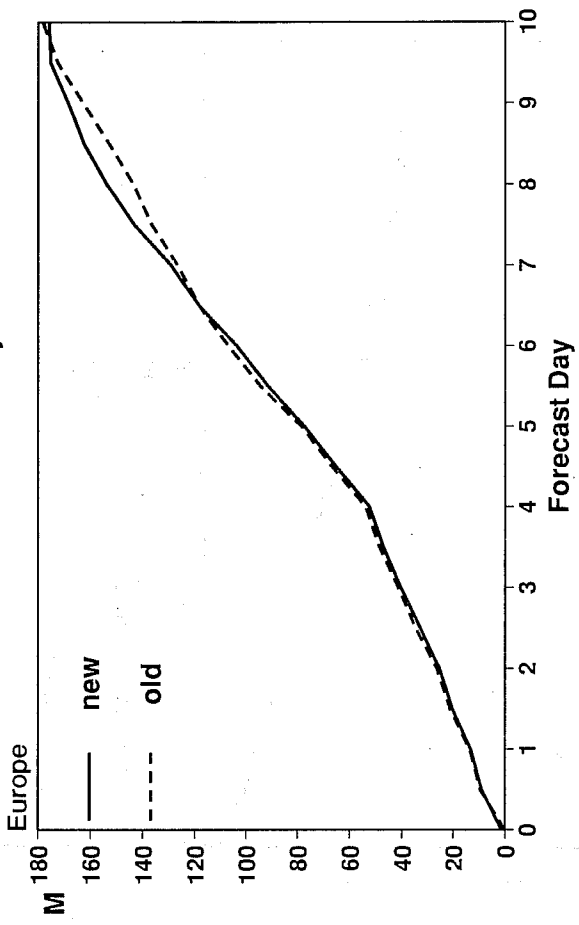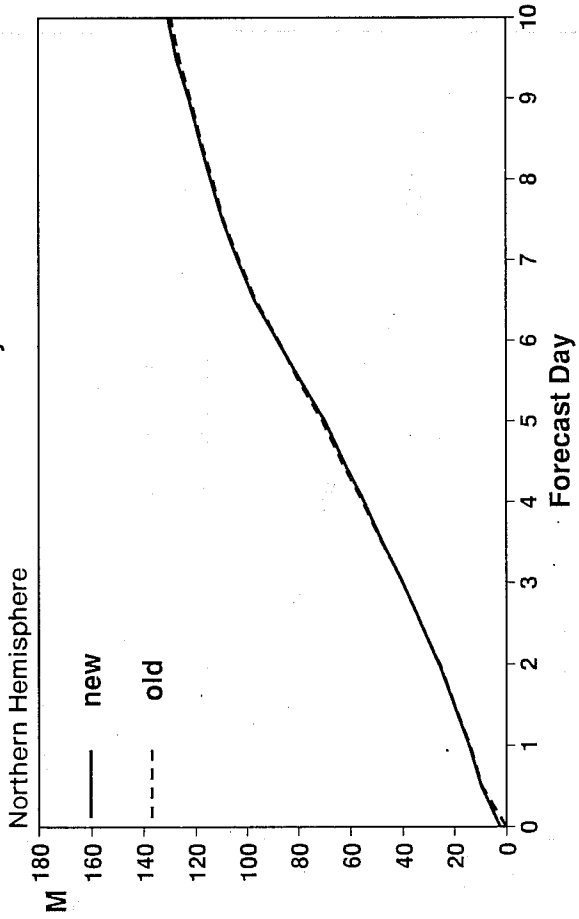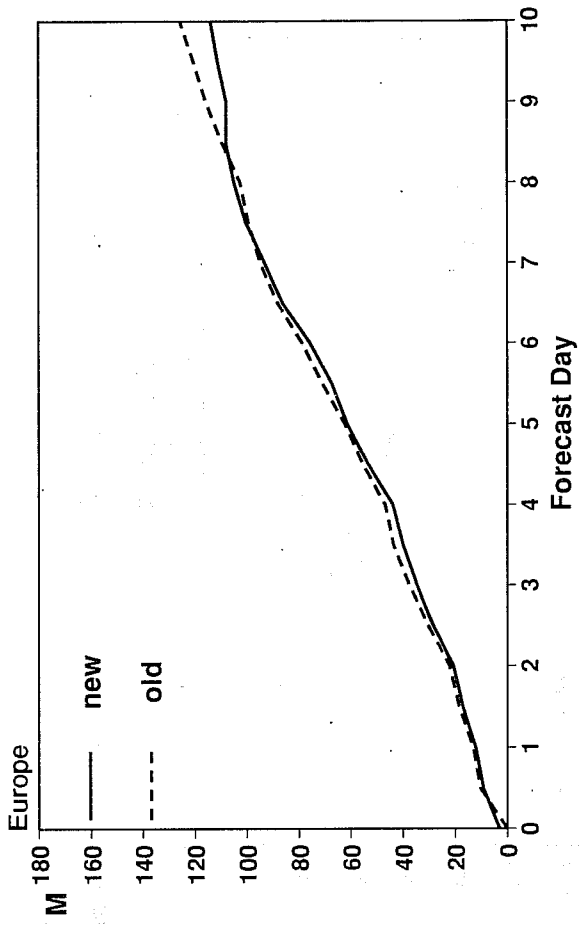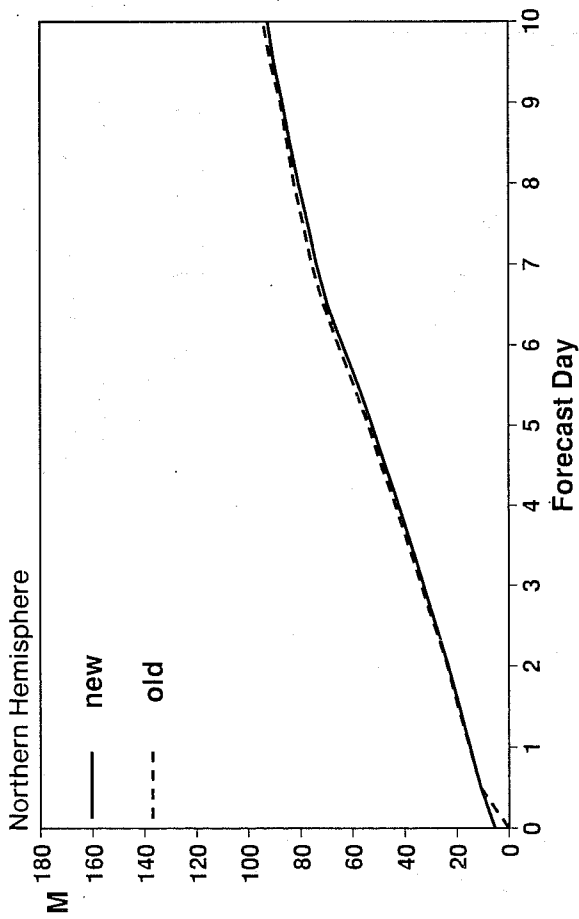
Fig 14b As Fig 14a but initial dates 94/03/03-94/03/16. Left column - N Hemisphere, right column - European area. Forecasts and assimilation with T213 system.
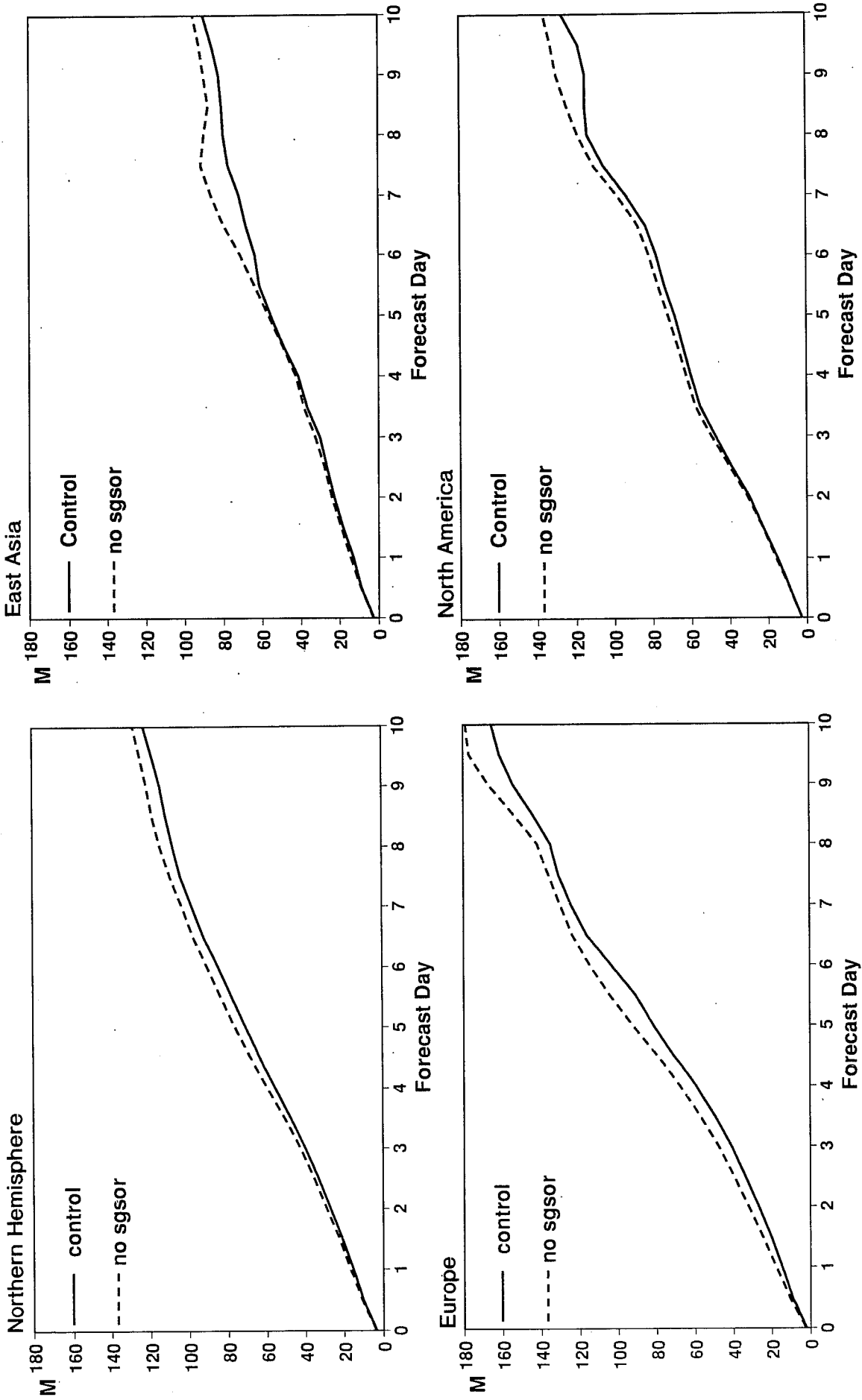
Fig 15 500 mb rms height errors for two sets of 19 T213 forecasts (with mean orography) with and without the new scheme
a) N Hemisphere, b) Europe, c) E Asia, d) N America.

31

APPENDIX 1: SPECIFICATION OF SUBGRIDSCALE OROGRAPHY

For completeness, the following describes how the subgridscale orography fields are computed in *Baines and Palmer* (1990). The mean topographic height above mean sea level over the grid point region (GPR) is denoted by $\bar{h}$ and the coordinate z denotes elevation above this level. Then the topography relative to this height $(h(x,y)-\bar{h})$ is represented by four parameters, as follows:

i) The net variance, or standard deviation μ of $h(x,y)$ in the GPR. This is calculated from the US Navy data set or equivalent, as described by *Wallace et al* (1983). μ gives a measure of the amplitude and 2μ approximates the physical envelope of the peaks (*Wallace et al*, 1983).

ii) A parameter γ which characterises the anisotropy of the topography within the GPR.

iii) An angle ψ, which denotes the angle between the low-level wind direction and that of the principal axis of the topography.

iv) A parameter σ which represents the mean slope within the GPR.

γ and ψ may be defined from the topographic gradient correlation tensor

$$H_{ij} = \overline{\frac{\partial h}{\partial x_i} \frac{\partial h}{\partial x_j}},$$

where $x_1 = x$, $x_2 = y$, and the terms may be calculated (from the USN data set) by using all relevant pairs of adjacent grid points within the GPR. This symmetric tensor may be diagonalised to find the directions of the principal axes and the degree of anisotropy. If

$$K = \left(\overline{\left(\frac{\partial h}{\partial x}\right)^2} + \overline{\left(\frac{\partial h}{\partial y}\right)^2}\right)/2, \quad L = \left(\overline{\left(\frac{\partial h}{\partial x}\right)^2} - \overline{\left(\frac{\partial h}{\partial y}\right)^2}\right)/2, \quad M = \overline{\frac{\partial h}{\partial x} \frac{\partial h}{\partial y}}, \tag{A1}$$

the principal axis of H_{ij} is oriented at an angle θ to the x-axis, where θ is given by

$$\theta = \tfrac{1}{2} \arctan(M/L). \tag{A2}$$

This gives the direction where the topographic variations, as measured by the mean square gradient, are largest. The corresponding direction for minimum variation is perpendicular. Changing coordinates to x', y' which are oriented along the principal axes ($x' = x \cos\theta + y \sin\theta$, $y' = y \cos\theta - x \sin\theta$)), the new values of K, L and M relative to these axes, denoted K', L' and M', are given by

$$K' = K, \quad L' = (L^2 + M^2)^{1/2}, \quad M' = 0,$$

where K, L and M are given by equation A1. The anisotropy of the orography or "aspect ratio" γ, is then defined by

$$\gamma^2 - \overline{\left(\frac{\partial h}{\partial y'}\right)^2} \Big/ \overline{\left(\frac{\partial h}{\partial x'}\right)^2},$$

$$- \frac{K'-L'}{K'+L'} - \frac{K-(L^2+M^2)^{\frac{1}{2}}}{K+(L^2+M^2)^{\frac{1}{2}}}. \tag{A3}$$

If the low-level wind vector is directed at an angle φ to the x-axis, then the angle ψ is given by

$$\psi = \theta - \varphi. \tag{A4}$$

The slope parameter, σ, is defined by

$$\sigma^2 - \overline{\left(\frac{\partial h}{\partial x'}\right)^2}, \tag{A5}$$

i.e. the mean square gradient along the principal axis.